SCIEPublish

Review

Recent Progress on Utilising Visible Light to Better Catalyst Stability for the Dry Reforming of Methane

George E. P. O'Connell, Rose Amal, Jason Scott * and Emma C. Lovell *

Particles and Catalysis Research Group, School of Chemical Engineering, The University of New South Wales, Sydney, NSW 2052, Australia; george.oconnell@student.unsw.edu.au (G.E.P.O.); r.amal@unsw.edu.au (R.A.)

* Corresponding author. E-mail: jason.scott@unsw.edu.au (J.S.); e.lovell@unsw.edu.au (E.C.L.)

Received: 23 December 2024; Accepted: 17 February 2025; Available online: 26 February 2025

ABSTRACT: Dry reforming of methane (DRM) is a promising strategy to closing the carbon loop. DRM valorises CO_2 and CH_4 by producing synthesis gas (H_2 and CO), the precursor to various synthetic fuels. Key limitations of the DRM are the high-temperature requirements (600–1000 °C) and competing side reactions, many of which produce carbon that can deactivate the catalyst. Designing a stable, low-cost and active catalyst remains one of the greatest DRM challenges. One potential strategy to curtail the limitations that hinder DRM is to utilise visible light to access the localised surface plasmon resonance (LSPR) of metal catalysts. The current review discusses the recent developments in designing catalysts for LSPR-assisted thermocatalytic DRM. The thermodynamic and kinetic principles that underpin DRM are first introduced, followed by an overview of thermocatalyst design strategies. The mechanism behind LSPR is discussed, with recent developments and strategies for introducing LSPR to the DRM examined. The review offers a thorough overview of catalyst design for light-assisted DRM and may be used as a guide to developing stable and light-receptive catalysts for the reaction.

Keywords: Dry reforming of methane; Visible light; Carbon formation; LSPR; Catalyst deactivation; Stability

1. Introduction

The current dependence on fossil fuels for energy has increased the atmospheric concentration of greenhouse gases such as carbon dioxide (CO_2) and methane (CH_4), stimulating a global temperature rise of 1.1 °C since 1850 [1]. The Paris Agreement in 2015 outlined the need to reduce carbon emissions by 45% to prevent a global temperature rise of 1.5 °C that would induce irrevocable climate damage [2,3]. The Sixth Assessment Report published by the Intergovernmental Panel on Climate Change in 2023 highlighted that the 2019 greenhouse gas release rates decreased relative to its last assessment in 2009, but the attempts to curb emissions were far below the Paris Agreement's requirements [1,2].

The need to mitigate the consequences of climate change has stimulated socio-political reform of the global energy platform. Current strategies to reduce CO_2 emissions focus on replacing fossil fuels as the primary energy source with green alternatives, preventative CO_2 capture and atmospheric CO_2 capture. Despite comparable technology costs, implementing green alternatives such as wind, solar and battery solutions fall short of the 45% CO_2 reduction target, so further developments in carbon capture, storage and utilisation projects are crucial to managing climate change.

As a strategy for mitigating climate change, CO_2 utilisation has great potential as the CO_2 feedstock may produce value-added chemicals. Currently, the infrastructure and energy costs required to overcome the stability of CO_2 limit widespread adoption [4]. Of these technologies, converting CO_2 to 'Green Fuels' (carbon neutral or negative net emissions) is highly promising. When combined with Fischer-Tropsch synthesis, the dry reforming of methane (DRM) reaction may produce various synthetic fuels via a synthesis gas intermediate (syngas, a combination of H_2 and CO) [5,6]. DRM contributes to valorising CO_2 by creating an intermediate gas mix product suited to producing fuels that may be substituted directly into existing infrastructure, particularly for the transportation industry (automobile, shipping or aviation fuels). Developing synthetic fuels from CO_2 creates a carbon loop with net zero emissions and without the

https://doi.org/10.70322/prp.2025.10004

infrastructure adaptability costs, providing a viable fossil fuel alternative.

DRM technology is less mature than other CO_2 conversion reactions like CO_2 methanation, as several challenges limit its technical and economic feasibility. The reaction's endothermicity requires high-temperature operation (600–1000 °C), necessitating significant energy input. At these temperatures, DRM competes with several side reactions, many of which deposit carbon that deactivates the catalyst. The DRM field is focused on strategies to improve the catalyst stability and lower the energy requirements [7,8]. One approach to overcome these thermodynamic limitations is to incorporate visible light in the DRM by inducing localised surface plasmon resonance (LSPR). Light-assisted DRM (thermal + visible light energy input) has demonstrated moderate improvements in low-temperature conversion, but has more recently been reported to considerably improve catalyst stability. Ultimately, the understanding of this strategy is far from comprehensive, limiting the potential of designing ideal light-receptive DRM catalysts.

Recent reviews addressing light incorporation into DRM focus on catalyst design for photothermal DRM, highlighting photo-enhancements achieved through bandgap and coupled bandgap-LSPR excitation [9,10]. These reviews highlight that semiconductor materials are required for bandgap excitation, and so recent developments focus on designing novel catalyst materials to improve photo excitation efficiency [11–13]. To date, no review article has examined the impact of incorporating LSPR to thermocatalytic DRM. Inducing LSPR in traditional thermocatalysts has demonstrated the potential to boost the catalytic performance of thermally active materials. This review examines the role of LSPR excitation in improving catalyst performance, focusing on the impact of light on the DRM reaction mechanism and catalytic stability. Understanding the mechanism behind the influence of light on catalyst stability is crucial to developing light-receptive catalysts. The current review initially discusses the thermodynamic and kinetic limitations of the DRM, where the current thermocatalytic design strategies, with an emphasis on stability, are considered. As illumination with visible light cannot provide sufficient energy to catalyse DRM, visible light illumination must be coupled with thermal heating, the main driving force for the reaction [14]. The materials and physicochemical properties that underpin thermocatalytic DRM are therefore fundamental to the performance of light-assisted DRM. The physics behind LSPR and methods to integrate visible light into DRM are discussed with recent developments in light-assisted DRM catalysts then reviewed, focusing on light's impact on catalytic stability. The review concludes with an analysis of the gaps in understanding and future work required to design an efficient, light-receptive catalyst for the conversion of CO_2 and CH_4 to syngas.

2. Reaction Chemistry and Thermodynamics

For the DRM reaction, CH_4 and CO_2 are combined over a heterogeneous catalyst (typically metal/metal oxide) to form syngas (Equation (1)) [5,15,16]. In addition to abating CO_2, DRM reduces the considerable water and energy input of the current syngas production route through the steam reforming of methane (SRM, Equation (2)) [17]. A stoichiometric H_2 and CO product ratio is formed under ideal reforming conditions (no side reactions), which may be converted into valuable hydrocarbons via Fischer-Tropsch synthesis [5]. Fischer-Tropsch synthesis with $H_2/CO \approx 1$ yields a variety of short and medium-chain hydrocarbons (38% C_{2-4} and 39% C_{5-11} yield over Fe_3O_4, T = 533 K, P = 1.50 MPa and t = 320 h), suitable for direct substitution into various oil-derived hydrocarbon applications [18].

$$CH_4 + CO_2 \rightleftharpoons 2CO + 2H_2 \quad \Delta H^0_{298\,K} = +247\ \text{kJmol}^{-1} \tag{1}$$

$$CH_4 + H_2O \rightleftharpoons CO + 3H_2 \quad \Delta H^0_{298\,K} = +206\ \text{kJmol}^{-1} \tag{2}$$

2.1. DRM Kinetics and Thermodynamics

The DRM reaction is endothermic, favouring reaction temperatures above 600 °C. These high temperatures are required to overcome the stability of CH_4, which is responsible for the high activation energy [19]. The reaction competes with several side reactions that impact the selectivity and deactivate the catalyst at typical reaction temperatures (600–1000 °C) [5,15]. Within this temperature range, DRM is highly susceptible to deactivation by carbon deposition reactions and active metal sintering [5,20,21]. DRM thermocatalyst design is centred on formulating a stable and selective catalyst that can effectively catalyse the reactants at relatively low operating temperatures (~500 °C).

Despite much research, the reaction mechanism remains contentious for common metal/metal oxide catalysts. The reaction mechanism depends on catalyst type, properties and reaction conditions. Although the reaction pathway depends on several variables, the activity of the support strongly influences the reaction performance [22]. Supports that have electron donation capacity (classified as 'Lewis basic' and 'active' supports) may be directly involved in the

reaction mechanism by providing CO_2 adsorption sites. Conversely supports with no mechanistic involvement are considered 'inactive' [22,23]. The most accepted mechanism was first proposed by Papadopoulou et al., drawing from several *in-situ* diffuse reflectance infrared Fourier transform spectroscopy (DRIFTS), density functional theory (DFT) calculations and kinetic studies that have since been supplemented by more recent work [5,16,24]. CH_4 adsorbs and dehydrogenates on the active metal surface, forming S_1–$CH_{x,ads}$ (S_1 = adsorption site '1') (Figure 1a.i). Simultaneously, CO_2 is adsorbed, disassociating into S_2–CO_{ads} on the metal oxide support or the active metal (S_2 = adsorption site '2'). The adsorption and disassociation of CH_4 and CO_2 are competitive on the active metal or active metal-support interface, where there is a greater charge concentration, particularly over inactive supports (absence of Lewis basic sites) [5,21]. CO_2 may also adsorb at the Lewis basic sites of active supports [5,21]. Once CO_2 and CH_4 are adsorbed, H_2 is formed by CH_x dehydrogenation, and both H_2 and CO are desorbed from the catalyst surface (Figure 1a.ii). In a slower process, S_1–$CH_{x,ads}$ is oxidised to form S_1–CO_{ads} (Figure 1a.iv) by either surface O_{ads} atoms or surface hydroxyls (OH_{ads}) formed by the coupling of surface H_{ads} and O_{ads} (Figure 1a.iii). The CO and H_2 are then desorbed. For this mechanism, the adsorption and disassociation of methane (CH_x–H bonds) are considered the rate-determining step (RDS) over a basic support [25–28].

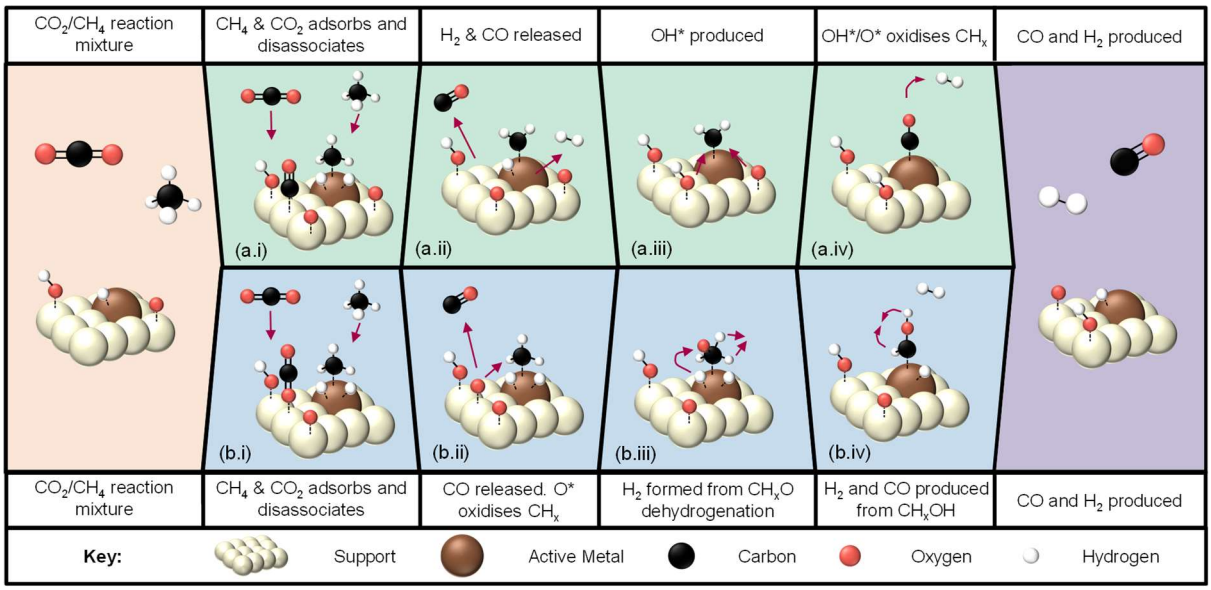

Figure 1. (**a**) The proposed dry reforming of methane reaction mechanism as described by Papadopoulou et al., whereby CH_x disassociation is considered the RDS (**a.i**) [24]. (**b**) The alternative 'methoxy' pathway, whereby either the CH_x intermediate forms CH_xO or carbonates adsorbed onto the support decompose to form CH_xO. Methoxy decomposition is considered the RDS (**b.ii**). The carbon, oxygen and hydrogen molecules are represented as black, red and white, respectively, and '*' denotes surface adsorbed material.

Other studies have suggested that the CH_xO intermediate ('methoxy species') may be a crucial intermediary species [24,29–31]. This species could form from the rapid oxidation of S_1–$CH_{x,ads}$ (produced from CH_4 dissociative adsorption onto the catalyst surface; Figure 1b.ii), which forms S_1–CH_xO_{ads}. The methoxy route differs from the previous pathway, where S_1–$CH_{x,ads}$ rapidly forms S_1–CO_{ads} upon oxidation. Alternatively, the methoxy intermediate may be formed by decomposing formate intermediates developed by CO_2 adsorbed onto the support. Literature suggests that the RDS for this methoxy pathway is the decomposition of the CH_xO intermediate to form CO and H_2 (Figure 1b.iii) [24,29]. This reaction pathway may improve stability relative to the primary pathway, as the early oxidation of CH_x may minimise the complete CH_x dehydrogenation that forms adsorbed carbon (C_{ads}) [31].

2.2. DRM Challenges

As mentioned previously, DRM is limited by the high reaction temperatures, competing side reactions and susceptibility to deactivation. Reaction modelling determined that up to nine side reactions may compete with the DRM reaction within the typical operating temperatures [32,33]. In addition to SRM (Equation (2)), the reverse Sabatier (Equation (3)), reverse water gas shift (RWGS, Equation (4)), Boudouard (Equation (5)), CH_4 cracking (Equation (6)) and hydrogen oxidation reactions (Equations (7) and (8)) are prevalent among these side reactions. Of these reactions, the Boudouard and CH_4 cracking produces carbon that may lead to catalyst deactivation. The impact of promoting RWGS is less severe than the carbon-forming reactions, as CO is a desired product for the DRM [17,22].

$$CH_4 + 2H_2O \rightleftharpoons 4H_2 + CO_2 \quad \Delta H^0_{298\,K} = +165\ kJmol^{-1} \tag{3}$$

$$CO_2 + H_2 \rightleftharpoons CO + H_2O \quad \Delta H^0_{298\,K} = +41\ kJmol^{-1} \tag{4}$$

$$2CO \rightleftharpoons CO_2 + C_{(s)} \quad \Delta H^0_{298\,K} = -172\ kJmol^{-1} \tag{5}$$

$$CH_4 \rightleftharpoons C_{(s)} + 2H_2 \quad \Delta H^0_{298\,K} = +75\ kJmol^{-1} \tag{6}$$

$$H_2 + CO \rightleftharpoons C_{(s)} + H_2O \quad \Delta H^0_{298\,K} = -131\ kJmol^{-1} \tag{7}$$

$$2H_2 + CO_2 \rightleftharpoons C_{(s)} + 2H_2O \quad \Delta H^0_{298\,K} = -90\ kJmol^{-1} \tag{8}$$

Equilibrium modelling (Figure 2a) [23] and Gibbs free energy modelling (*i.e.*, reaction spontaneity, Figure 2b) [34] show that the Boudouard reaction occurs primarily below 700 °C. CH_4 cracking typically occurs above 550 °C, indicating that all three side reactions coincide at low operating temperatures (500–700 °C). The low thermal energy input, competing side reactions and potential carbon deposition through the Boudouard and CH_4 cracking reactions make thermocatalyst design challenging for low-temperature DRM.

The product ratio (H_2/CO) can directly observe the impact of side reactions. Under ideal operating conditions, this ratio should be stoichiometric (1/1). The RWGS will result in a significant decrease in H_2/CO ratio (<1) as H_2 is consumed and CO is produced [5,33]. The Boudouard reaction and CH_4 cracking cause an increase in H_2/CO ratio (>1) as CO is consumed or H_2 is produced [5,33,35]. Whilst the H_2/CO ratio is a key parameter in understanding catalyst performance for the DRM, it does not provide a complete understanding of the system, as several side reactions are likely to occur simultaneously.

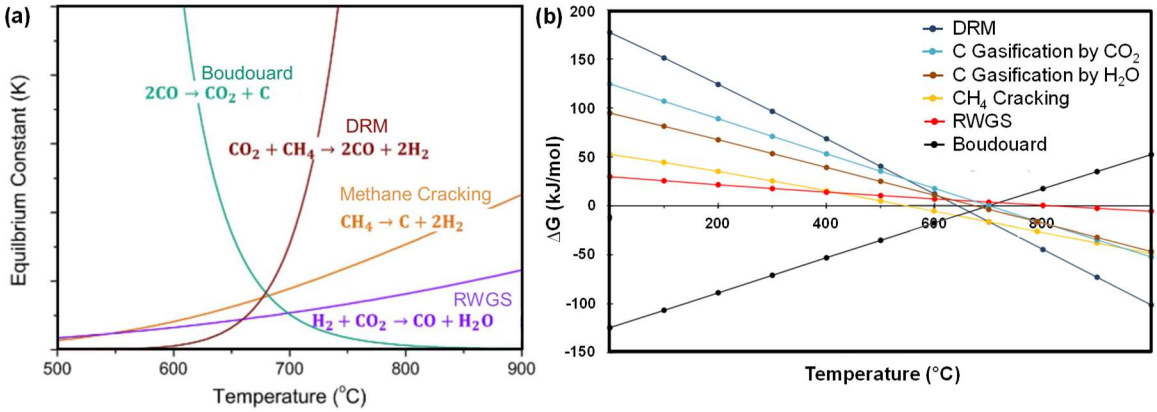

Figure 2. Temperature dependence of DRM side reactions on (**a**) the equilibrium conversion and (**b**) Gibbs free energy, showing the prevalence of side reactions for the low-temperature DRM (500–700 °C). Image (**a**) adapted with permission from Lovell et al. [23]. CC 4.0. Image (**b**) adapted with permission from Abdulrasheed et al. [34]. CC 3.0.

DRM catalysts are often deactivated by carbon deposition (or 'coking') through the Boudouard and/or CH_4 cracking reactions or catalyst sintering. Carbon-driven deactivation may occur through several mechanisms, including forming surface metal carbides, encapsulating active sites and plugging of support pores (and/or the reactor), all leading to an activity decrease by limiting access to active sites [36–38]. Additionally, whisker carbon may be formed between the active metal and the support. The whisker does not directly deactivate the catalyst, with the loss in activity deriving from a diminished metal-support interaction (MSI) and reactor clogging [17,37]. The formation of different carbon types depends on the catalyst and reaction conditions. Surface atomic carbon (type 'α') and amorphous films and filaments (type 'β') are 'active' carbon, where available adsorbed oxygen atoms may gasify the species to form gaseous CO (Figure 3). With insufficient O_{ads}, excessive carbon build-up may lead to graphitic (type 'C') carbon formation [37,38]. For some active metals, particularly non-noble transition metals like Ni and Co, carbon may diffuse through the active metal, accumulating between the metal and the support, forming carbon nanotubes ('whiskers', type 'ν') with the active metal at the head [37,38]. Over Ni-based catalysts, nickel carbide (Ni_3C, type 'γ') may form through the reaction of surface C with the active metal [37].

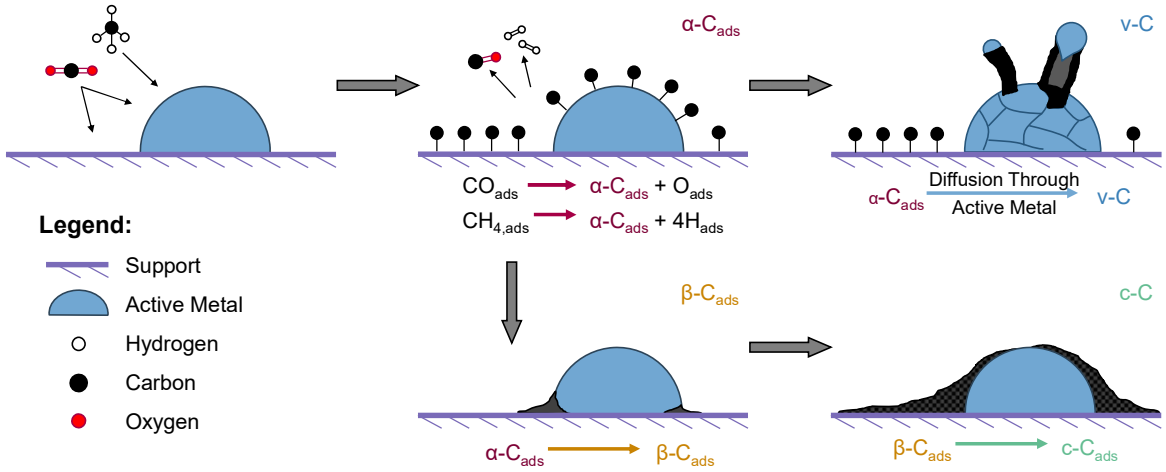

Figure 3. Possible carbon formation mechanisms, identifying the formation routes of α (red), β (yellow), ν (blue) and c (green). Of these carbon species, α and β carbon are considered 'active' as they may be gasified by surface-adsorbed oxygen.

Deactivation may also occur through sintering of the active metal. At higher reaction temperatures (often above 700 °C) [16], adjacent active metal deposits may agglomerate, forming larger deposits with a lower surface area that inhibits surface adsorption [39]. Deactivation by sintering and coking may occur simultaneously, as larger particle sizes often stimulate carbon deposition [39,40]. Deactivation may be minimised by carefully considering operation conditions and catalyst design, which will be discussed in Section 3.4.

3. Thermocatalyst Design

While this review is focused on the impact of light on DRM stability, the catalyst design strategies for light-assisted DRM are adapted from thermocatalytic DRM. As light is used to supplement the thermal energy input and boost the performance of thermal DRM, outlining the approaches to thermocatalyst design is crucial to justifying the materials and properties for light-assisted DRM. This section provides an overview of thermocatalyst design, as this has been addressed in-depth in other reviews [5,15,21].

Conventional DRM thermocatalysts employ an active metal loaded on a metal oxide support (Figure 4) [23,41]. The active metals are categorised as noble metals, like platinum (Pt), palladium (Pd), rhodium (Rh) and ruthenium (Ru), or non-noble metals, like nickel (Ni), cobalt (Co) and iron (Fe). Similarly, a range of supports have been employed for these reactions. In addition to providing essential mechanical stability, the support considerably influences catalytic performance by providing the surface area necessary for active metal stabilisation and dispersion [21,22]. Ceria (CeO_2), lanthana (La_2O_3), zirconia (ZrO_2) and magnesia (MgO) are considered active, as they contain Lewis basic sites that assist with the adsorption of the acidic CO_2. Other supports, such as silica (SiO_2), alumina (Al_2O_3), and yttria (Y_2O_3), are classified as inactive [21,23]. Titania (TiO_2) is another common support that has been classified as both active and inactive, depending on the extent of TiO_x formation upon surface reduction of TiO_2 [42,43]. Recent trends in thermocatalyst design introduced emerging support materials such as activated carbon, clay, silicon carbide (SiC), boron nitride (BN) and metal-organic frameworks, which are not discussed in this review [22].

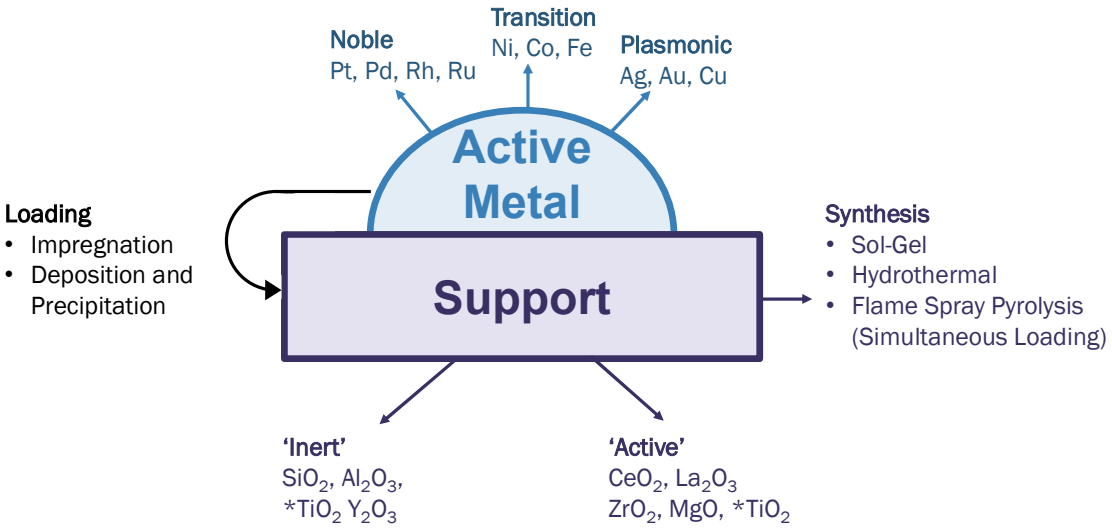

Figure 4. Various aspects of thermocatalyst design, including active metal and support selection, synthesis and active metal loading techniques. * Note: TiO_2 may be classified as an active or inactive support depending on the role of the TiO_x surface layer in the DRM reaction mechanism. Image adapted with permission from Lovell et al. [23]. CC 4.0.

Thermocatalysts are designed to be active, selective and stable (the three primary performance criteria). The performance is controlled by the active metal and support material properties, synthesis technique, preparation conditions such as the calcination temperature (when required) and the reduction conditions (the active metal should be fully reduced to provide the necessary surface properties and electronic structure to facilitate the reaction) [23].

3.1. Role and Selection of Active Metals

The active metal is the principal component of the catalyst that facilitates the DRM reaction. For an active support, CH_4 adsorbs and disassociates on the active metal. The active metal also provides CO_2 adsorption sites, particularly for inactive supports [21,22]. The material selection and the active metal physicochemical properties like deposit size, dispersion and loading all impact catalyst performance. As mentioned previously, noble (Pt, Pd, Rh and Ru) and non-noble metals (Ni, Co, Fe) are employed for the DRM. Noble metals are desirable, as they are active and highly stable, with excellent resistance to coking and high-temperature sintering [21]. The cost of noble metals is orders of magnitude greater than non-noble metals, too great to justify commercialisation [44,45]. Non-noble metals are favourable for their low-cost and high affinity, so thermocatalyst design typically focuses on improving non-noble metal performance [21,22].

Hou et al. demonstrated the performance of the active metals on mesoporous α-Al_2O_3 for DRM (T = 800 °C, WHSV = 60 $L \cdot g_{cat}^{-1} \cdot h^{-1}$, t = 240 min) [46]. Of the common active metals, Ni, Co and Pd deposited carbon, resulting in catalyst deactivation. Conversely, Rh, Ru and Pt had negligible carbon deposition (0.00 $mg_c \cdot g_{cat}^{-1} \cdot h^{-1}$), demonstrating the high stability of noble metals [46]. The activity followed the order Ni > Co ≈ Rh > Ru > Pd > Pt, though the Ni and Co used a higher loading (10wt% compared to 5wt% for noble metals), which likely influenced the results [46]. The high activity and low cost of Ni and Co drive their use in thermocatalytic DRM despite their susceptibility to carbon deposition [5,37].

Ni is both active and selective for the DRM [21,46]. Within the DRM operating temperatures (600–1000 °C) [5], Ni becomes susceptible to sintering and carbon deposition, deactivating the catalyst. Relative to other metals, Ni has a low Tammann temperature (when the bulk atoms become mobile, resulting in atomic reorganisation) of 590 °C [47], causing sintering within the low-temperature DRM range (500–700 °C) [48,49]. Ni sintering deactivates the catalyst by lowering Ni dispersion, which may be slowed or prevented by stabilising the active metal on the support and increasing the support surface area to improve Ni dispersion [50,51]. Deactivation through carbon deposition may be caused by poor carbon gasification rates (oxidising carbon to form CO or CO_2 gas products) due to strong Ni-C bonding [52,53] or high carbon diffusion rates through the active metal that yields whisker-type carbon [37]. Overcoming the considerable carbon deposition and preventing Ni sintering are the greatest challenges for Ni-based catalysts for DRM, particularly as carbon formation is often linked to metal dispersion [22,24,29].

Like Ni, Co is an active and inexpensive transitional metal [41,44]. There are conflicting reports in literature when comparing the activity of Co and Ni, where several studies identified Ni as more active [54–56], while others have suggested that Co is more active [48,57]. Like Ni, Co also suffers from deactivation through coking and sintering,

although Co sintering usually occurs outside the low-temperature DRM range (typically above 700 °C) [16]. Similarly, Co has exhibited better coke resistance than Ni, which several authors attribute to the improved resistance to stronger O_{ads} adsorption, improving the O availability to gasify surface carbon [48,56,58].

The active metal loading, deposit size, and dispersion are three inextricably linked physicochemical properties that may be controlled by varying aspects of catalyst synthesis, such as precursor concentrations, synthesis technique, temperature treatment and MSI. Generally, greater DRM activity is achieved ≥10 wt% metal loading, but beyond 10 wt% typically exhibits similar performance [21,59]. A study on xCo/MgO by Wang et al. demonstrated that loadings from 8–36 wt% (8, 12, 24, 36 wt%) had comparable CO_2 and CH_4 conversions, which was greater than the 4 wt% Co/MgO catalyst. A loading of 48 wt% had the same initial conversion, although the catalyst rapidly deactivated, attributed to large metal clusters that facilitated carbon deposition [60]. Without careful synthesis control, increasing the metal loading decreases the dispersion due to active metal agglomeration, which may facilitate active metal sintering [51,61,62].

Smaller deposit sizes are more active, selective and stable for DRM [51,63]. Most significantly, several studies identified a size threshold for whisker carbon formation, though the value depended on the materials and conditions employed in the studies [21,51,63]. Damaskinos et al. used $Ni/Ce_{0.8}Ti_{0.2}O_{2-\delta}$ to show that beyond a threshold value (Ni size = 22 nm), Ni facilitated both carbon deposition reactions (primarily CH_4 cracking) [63]. Smaller Ni deposits (<22 nm) accelerated carbon gasification through better CO_2 disassociation and greater access to CeO_2 labile oxygen atoms, improving carbon resistance [63]. Metal sintering that increases the particle size through agglomeration also stimulates carbon deposition via the mechanism outlined by Damaskinos, which impedes DRM performance. Similarly, Zhan et al. studied the impact of Ni size over Mg(Al)O solid solution for various reduction (650–800 °C) and reaction (500–800 °C) temperatures [51]. Increasing the reduction temperature beyond the Ni Tammann temperature induced sintering, increasing the Ni deposit size. For reaction temperatures between 500–700 °C, small deposits (5.8 nm) were active, while deposits ≥6.6 nm were deactivated due to whisker carbon formation (Figure 5) [51], demonstrating that the whisker carbon size threshold (~6 nm) varies considerably between materials. The strength of MSI is a crucial factor in designing thermocatalysts for the DRM. Strong MSI promotes active metal dispersion and stabilisation, which may prevent or limit the sintering extent of the active metal that would otherwise deactivate the catalyst [17,64]. Conversely, weaker MSI yields larger active metal sizes for DRM. The larger sizes improved CH_4 turnover, promoting H-spillover as well as facilitating CH_4 cracking, indicating that the MSI must be carefully controlled to optimise performance [17].

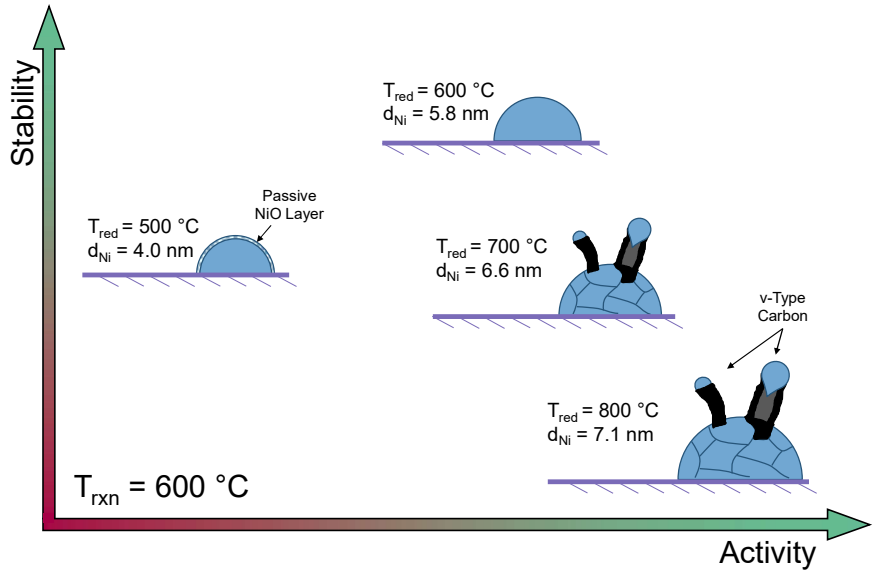

Figure 5. Summary of the Ni deposit size study by Zhan et al. over a Mg(Al)O support [51]. Increasing the reduction temperature induced Ni sintering. Small sizes (5.8 nm) were active at low DRM temperatures (500–700 °C), while increasing the Ni size to 6.6 nm induced whisker carbon formation and catalyst deactivation.

3.2. Role of Supports

Active metals loaded onto metal oxides Al_2O_3, CeO_2, SiO_2, and TiO_2 are the most employed heterogenous catalysts for the DRM. Other supports, such as yttria (Y_2O_3), zirconia (ZrO_2) and magnesia (MgO), are more commonly used as dopants to overcome the limitations of inert supports as they are less effective as stand-alone supports. Y_2O_3 and ZrO_2 weakly interact with the active metal, resulting in poor active metal dispersion and sintering susceptibility [65,66].

Conversely, MgO promotes strong MSI while providing poor surface area, yielding low active metal dispersion [65,66]. Recent work has utilised various carbon-based compounds, metal-organic frameworks, clay, and boron nitride as DRM catalyst supports [22]. Recent reviews have thoroughly addressed the design of novel materials for thermocatalytic DRM, so these materials are not considered in this review [22,67]. As previously detailed, these conventional supports can be classified as inactive (Al_2O_3, SiO_2, TiO_2*) or active (TiO_2*, CeO_2 and ZrO_2), depending on the role of the support in the reaction mechanism.

As a DRM catalyst support, Al_2O_3 has been heavily studied, exhibiting mild activity relative to other supports [65,66]. It is often favoured for its good thermal and mechanical stability and high surface area, facilitating active metal dispersion [21,68]. Al_2O_3 exists in several stable crystalline phases, most commonly alpha (α-Al_2O_3), gamma (γ-Al_2O_3) and eta (η-Al_2O_3) alumina [69]. $NiAl_2O_4$ or $CoAl_2O_4$ spinel formation is common, particularly upon high-temperature calcination or high-temperature operating conditions (>700 °C) [70,71]. The spinels form due to the strong MSI and are undesirable as they limit the availability of active species, impeding catalyst performance. In the absence of aluminate spinels, strong MSI with Al_2O_3 supports has been shown to restrict the complete reduction of Ni or Co, which hampers catalyst activity [70,71]. Alumina-supported Ni and Co rapidly deactivate through carbon deposition, often attributed to the active metal properties. Al_2O_3 is an irreducible support and, therefore, has a limited capacity to release O species to gasify the surface carbon, resulting in carbon accumulation [21,60].

Like Al_2O_3, SiO_2 is used for its high surface area, thermal stability, and low cost compared to other supports [21,72]. Typically, SiO_2 has no CO_2 adsorption capacity, so the activity is mainly attributed to the active metal properties. Silica is also highly desirable for its controllable porosity and morphology, whereby non-porous, mesoporous and core-shell structures are commonly employed [21,73]. The initial DRM performance of non-porous SiO_2 is amongst the most active supports, although it is susceptible to catalyst deactivation by active metal sintering induced by poor MSI [65,66]. Several studies reported carbon-driven deactivation, making non-porous SiO_2 non-functional for high-temperature DRM. Mesoporous or core-shell structures demonstrate improved sintering resistance and prevent whisker carbon formation [74,75]. Changing the porosity alone has been shown to be insufficient to mitigate carbon formation entirely, as the catalysts produced graphitic and amorphous carbon that deactivated the catalyst by pore blocking [37,74,76].

Classifying TiO_2 as an active or inactive support typically depends on the MSI strength. Titania with strong MSI partially encapsulates the active metal with a reducible TiO_x layer [42,43]. The TiO_x layer may provide sites for CO_2 adsorption, resulting in highly active catalysts [42,43] (Figure 6a). Nagaoka demonstrated that releasing oxygen trapped in the TiO_x basic sites facilitated carbon gasification, improving the stability of the DRM [42]. The extent of TiO_x encapsulation is dependent on the MSI. With very strong MSI, extensive coverage may prevent reactant adsorption on the active metal, rendering the catalyst inactive [43]. As strong MSI induces the active TiO_x layer, weak MSI yields an inactive TiO_2 support often characterised by moderate DRM activity and poor stability (limited support oxygen release capacity) [65,66]. Relative to the other supports, TiO_2 often has a low surface area, resulting in poor active metal dispersion [65,66]. Additionally, TiO_2 commonly undergoes a phase change from anatase (a-TiO_2) to rutile (r-TiO_2) around 600 °C, provoked by either high-temperature calcination or the DRM reaction temperatures [77]. The influence of this catalytic performance for DRM was not severe, whereby Shah et al. demonstrated that the r-TiO_2 phase was marginally less active than a-TiO_2 [78]. TiO_2 has potential for the DRM, and current work focuses on using promoters and dopants to boost the support surface area and induce basicity on inactive TiO_2 [17,22].

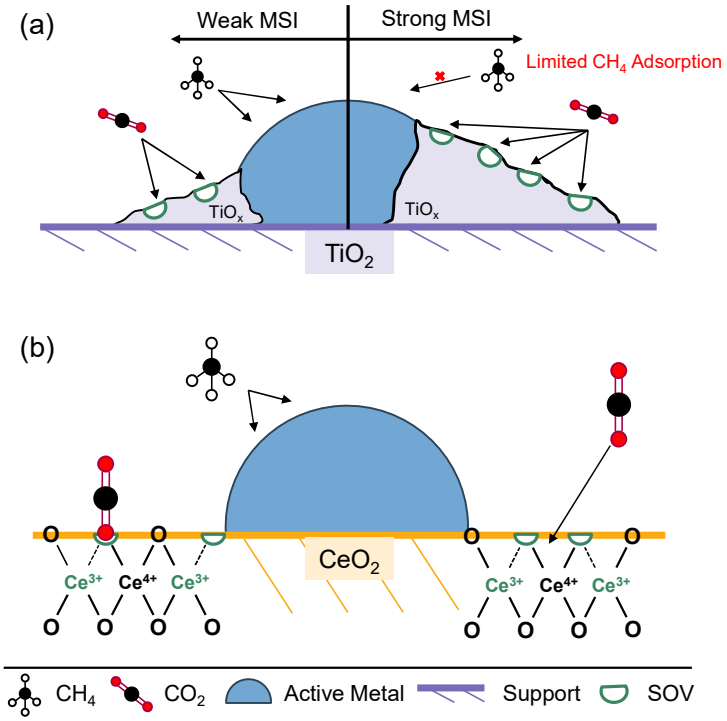

Figure 6. (**a**) Classification of TiO_2 as 'active' or 'inactive' depends on the presence of the TiO_x. Surface oxygen vacancies (SOVs) may aid the absorption of CO_2. Small quantities of this TiO_x layer is advantageous for assisting CO_2 adsorption, but extensive coverage of the active metal from strong metal support interaction (MSI) may prevent access to the active metal for CH_4 adsorption and disassociation. (**b**) Surface CeO_2 is highly reducible, allowing the facile generation of SOVs at Ce^{3+} sites. These sites aid the adsorption of the CO_2 molecule.

CeO_2 is a promising support that has demonstrated excellent coke resistance. The support is characterised by high oxygen storage capacity, distinctive redox properties, and often forms strong MSI with transitional metals, limiting active metal sintering [5,22]. CeO_2 undergoes a facile transition between Ce^{4+} and Ce^{3+} oxidation states arising from a single weakly bound f-shell electron [79,80]. The electron structure makes CeO_2 highly reducible, whereby low-temperature surface reduction occurs from 200–400 °C and bulk reduction from 650 °C [81]. Surface oxygen vacancies (SOVs) are formed upon reduction, which may have one or two unpaired electrons (Lewis basic sites) that aid CO_2 adsorption (Figure 6b) [82]. Despite the benefits, Wang et al. showed that CeO_2 was less active than the supports considered thus far, achieving a maximum CO_2 conversion of 63.2% (compared to 87.4%, 88.2% and 65.7% for Al_2O_3, SiO_2 and TiO_2, respectively) and CH_4 conversion of 50.7% (compared to 82.1%, 82.3% and 50.1% for Al_2O_3, SiO_2 and TiO_2, respectively—0.5 wt% Rh catalyst, T = 800 °C, WHSV = 60 $L \cdot h^{-1} \cdot g^{-1}$) [65]. Selected studies have shown that negligible carbon deposition may occur over CeO_2 [17,80]. The release of O_{ads} captured in the SOVs on ceria (often referred to as 'labile O') presents an opportunity to improve DRM stability, whereby the released O_{ads} may gasify surface carbon to form CO. Isotopic experiments using ^{18}O directly showed the contribution of lattice oxygen to CO formation by carbon gasification [63,83–85]. Damaskinos et al. demonstrated over $Ni/Ce_{0.8}Ti_{0.2}O_2$ that the transient release of labile O was faster than CO_2 disproportionation over Ni, preventing carbon build-up and thereby achieving a stable catalyst [63]. Carbon accumulation is impacted by several compounding variables, including the rate and quantity of oxygen released from CeO_2, the carbon diffusion rate through the active metal, the amount of carbon accumulated at the metal-support interface and the exposed active metal crystallite phase [83]. If the carbon gasification rate by the release of trapped O_{ads} does not exceed the carbon deposition rate, then the carbon will accumulate, irrespective of the oxidative capacity of the support.

3.3. Synthesis Techniques

The physicochemical properties of the catalyst are predominantly dependent on the material selection. However, varying the synthesis technique may allow the fine-tuning of physical and chemical properties such as the active metal deposit size, active metal dispersion, MSI and the catalyst reducibility [7,86]. While the synthesis technique is crucial to achieving desired material characteristics and properties, the benefits of various techniques have been explored extensively in other thermocatalytic DRM reviews [17,21] and will not be discussed in this review.

3.4. Thermocatalytic Stability Improvement Strategies

The greatest limitation of DRM is the catalyst instability caused by active metal sintering or coke deposition. Manipulating the operating conditions and catalyst design are possible methods to improve thermocatalyst stability.

3.4.1. Influence of Operating Conditions

The reaction temperature, pressure, and CO_2/CH_4 feed ratio are all optimisable parameters to limit carbon deposition [87]. As discussed in Section 2, the catalyst is susceptible to deactivation by carbon deposition between 500–700 °C. Thermodynamic modelling determined that 525–625 °C favours carbon deposition through the Boudouard reaction, and CH_4 cracking occurs from 550 °C, making temperature optimisation difficult. Literature suggests that operating the DRM at 700 °C is preferred, as greater temperatures stimulate CH_4 cracking, and lower temperatures initiate the Boudouard reaction [21,33]. A computational study by Nikoo et al. found that pressures above 1 atm increased the carbon deposition across all temperatures [33], which was supported by Wang et al., who demonstrated better DRM conversions at low pressures (0.01 atm) [88].

Literature suggests that changing the CO_2/CH_4 ratio from stoichiometric 1/1 may limit carbon formation reactions at certain temperatures [33]. Increasing the ratio (*i.e.*, CO_2-rich feed) improved the CH_4 conversion, achieving near-complete conversion by 800 °C. Increasing the CO_2/CH_4 ratio creates a soft oxidative environment that promotes CH_4 oxidation, preventing carbon deposition by CH_4 cracking [33]. Furthermore, increasing the ratio limited CO_2 conversion, particularly below 600 °C [33]. Arora et al. suggested that the exothermic hydrogen oxidation reaction (Equation 8) caused this decrease while simultaneously depositing carbon [38]. The DRM reaction became favoured from 700 °C, and by 800 °C, the CO_2 conversion neared completion for low CO_2/CH_4 ratios. As altering the system pressure and CO_2/CH_4 ratio changes the DRM environment and balance of side reactions, the product ratio (H_2/CO) and reaction consumption are ultimately changed, as stoichiometry dictates a 1/1 conversion. Literature instead focuses on catalyst design strategies to overcome carbon deposition under atmospheric pressure and a stoichiometric CO_2/CH_4 feed ratio.

3.4.2. Stability Considerations in Thermocatalyst Design

As previously established, many DRM catalysts are susceptible to carbon deposition. Consequently, much work has focused on tuning and modifying the catalysts to be more stable toward DRM. The design of a stable catalyst has been centred around three possible strategies; (i) using two active metals ('bimetallic'), (ii) using a promoter; and (iii) altering support basicity.

As discussed in Section 3.1.1, noble metals such as Pt, Ru and Rh are highly stable for DRM, producing negligible carbon. Selected studies showed that incorporating small quantities of noble metal improved the stability of a non-noble catalyst. Moreno et al. highlighted that 2 wt% Ru decreased the carbon formation of Ni/Al_2O_3 by 27%. Decreasing the Ru concentration to 0.5 wt% resulted in a 66% decrease in carbon formation while increasing the catalytic activity (750 °C, WHSV = 110 $L \cdot h^{-1} \cdot g^{-1}$) [89]. The 2 wt% Ru sample formed large Ru agglomerates (~38 nm) that had poor interaction with Ni (~8 nm), but 0.5 wt% Ru greatly interacted with Ni, improving stability [89]. The authors did not investigate the Ni–Ru interaction that caused the improved stability. Li et al. performed a comprehensive review of the impact of noble promotion on DRM and found that small amounts of noble metals consistently modified the surface electronic properties of Ni, leading to carbon resistance. Introducing noble metals resulted in smaller, more stable Ni deposits that resisted sintering [90]. Horlyck et al. demonstrated the potential of non-noble metal bimetallic catalysts by synthesising several $Ni–Co/Al_2O_3$. The study showed that Ni was susceptible to both Boudouard and CH_4 cracking reactions, but Co was susceptible to only the Boudouard (600 °C, WHSV = 144 $L \cdot h^{-1} \cdot g^{-1}$). The authors found that small amounts of Co (2.5 wt%) alloyed with Ni (7.5 wt%) stimulated facile electron transfer that aided the oxidation of carbon species, resulting in a significant reduction in carbon deposition (96% relative to $10Ni/Al_2O_3$) [56]. As Ni–Co costs much less than noble metal promotion, new studies focus on optimising these bimetallic non-noble catalysts [37,56].

Promoters differ from bimetallic catalysts, as the promoter is typically inactive toward DRM but instead alters the catalyst properties to improve DRM performance. A wide range of metals have been assessed for DRM. Franz et al. studied the promotion impact of alkali earth metals (Na, K and Cs) on a $10Ni/ZrO_2$ catalyst [91]. Introducing the promoters decreased the initial CH_4 conversion from 50% for $10Ni/ZrO_2$ to ~40% with 1 wt% promoters and further to ~30% with 2 wt% promoters (regardless of promoter material). The alkali promoter reduced the carbon content from 53 $mg_c \cdot g_{cat}^{-1}$ for $10Ni/ZrO_2$ to ≤10 $mg_c \cdot g_{cat}^{-1}$. A promoter content of 1 wt% was able to reduce carbon content, although the CH_4 conversion decreased by 10%, limiting its potential. Increasing the promoter content to 2 wt% reduced the carbon content below 5 $mg_c \cdot g_{cat}^{-1}$, while the activity decreased by 20% relative to $10Ni/ZrO_2$. The authors attributed

the stability improvements to the formation of carbonates on Na and Cs (Na_2CO_3 and Cs_2CO_3), which are known to promote carbon gasification over alkali metals [91–93]. Ibrahim et al. studied the influence of 1 wt% Ga, Gd, Sc, Ce and Cs on 5Ni/MCM-41 (mesoporous silica) [94]. Ce, Ga and Gd improved the activity considerably, which was attributed to improved basicity relative to the 5Ni/MCM-41 control. Although Cs and Sc deactivated the catalyst by oxidising Ni, all the promoted catalysts exhibited a lower carbon deposition. Several studies have demonstrated the impact of B promotion, which has been shown to increase the basicity by inducing hydroxyl groups, which enhances catalytic activity [95–97]. Additionally, Fouskas et al. showed that B promotion (<5.6 wt%) may also reduce the Ni size, improving carbon resistance by up to 86% [96].

The final commonly studied approach to enhance DRM catalyst stability is to synthesise mixed oxides to improve support basicity. Modifying Al_2O_3 with basic oxides presents an opportunity to overcome carbon deposition. Horváth et al. showed that a ~9 wt% CeO_2 content resulted in a small decrease in the activity while significantly reducing the carbon deposition rate (by ~70%), causing a considerable stability improvement [98]. Laosiripojana et al. varied the Ce concentration from 0 to 14 wt% for Ni/Al_2O_3-CeO_2 [99]. They found that the Ce did not influence the Ni properties, and the CO_2 incorporation increased the activity relative to Ni/Al_2O_3 (T = 900 °C). Like Horváth, they found that incorporating CeO_2 improved coking resistance, whereby negligible carbon was formed above 8 wt% Ce. Similarly, MgO has enhanced the DRM performance of Al_2O_3-supported materials while suppressing carbon formation [100], although high-temperature calcination risks $MgAl_2O_4$ formation, which was more active than Al_2O_3 but was unstable due to coking [101].

Other studies modified the support to improve the reducibility and oxygen storage capacity of reducible oxides, like CeO_2, to further enhance the support anti-coking properties. Incorporating Zr into CeO_2 ($Ce_xZr_{1-x}O_{2-\delta}$, or 'CZx') forms a Ce–Zr solid solution that improves the thermal stability, promotes the facile production of SOVs and improves oxygen storage and transport [102]. Despite the improved surface basicity, incorporating Zr resulted in whisker carbon formation for the DRM [102,103]. The mechanism behind carbon deposition in the presence of Zr has not been investigated, but it occurred irrespective of Zr content [102]. Vasiliades et al. incorporated Pr into CeO_2 ($Ce_{1-x}Pr_xO_{2-\delta}$, where x = 0, 0.2, 0.5, 0.65, 0.8, 5 wt% Ni loading) as an alternative to Zr. Increasing Pr content negated carbon formation but decreased the DRM activity (Table 1). The lowest Pr modification ($Ce_{0.8}Pr_{0.2}O_{2-\delta}$) displayed similar activity to Ni/CeO_2 and had better carbon resistance, which was attributed to the greater oxygen storage capacity and mobility upon Pr lattice substitution [104]. Modifying irreducible and reducible supports may offer a way to tailor a catalyst to be stable and selective to the DRM reaction.

Table 1. Summarised performance of Pr-modified CeO_2 catalysts in a study by Vasiliades et al. [104].

Catalyst	Temp (°C)	Conversion (%) [a]		Carbon Formation	
		CO_2	CH_4	Total Carbon (wt%) [b]	Moles of Active Carbon (μmolg^{-1}) [c]
5 wt% Ni/CeO_2	550	19	12	-	3.7
	750	85	80	19.6	88
5 wt% Ni/$Ce_{0.8}Pr_{0.2}O_{2-\delta}$	550	19	12	-	0.72
	750	82	75	0.22	2.0
5 wt% Ni/$Ce_{0.2}Pr_{0.8}O_{2-\delta}$	550	13	6	-	0.87
	750	63	50	0.07	16.7

[a] P = 1 bar, GHSV = 30,000 h^{-1}. [b] Determined by thermal gravimetric analysis after 25 h at 750 °C, GHSV = 30,000 h^{-1}. [c] Active carbon measured by isotopic *in-situ* DRIFTS.

4. Localised Surface Plasmon Resonance

Integrating solar illumination (ultraviolet, visible light, and infrared) may help solve the DRM limitations. Providing kinetic and thermodynamic assistance from electromagnetic radiation (EMR) may offset the thermal requirements and promote specific DRM reaction pathways [55,85]. Several avenues of solar illumination have been explored in literature. Xie et al. outlined the definitions of each illumination approach, which contain nuance in the mechanisms that drive the reaction [105]. The avenues of integrating light into DRM are summarised in Figure 7. 'Photocatalysis' describes the direct conversion of CO_2 using light as the only energy source (*i.e.*, no thermal heating). Semiconductor bandgap excitation by photon adsorption creates electron-hole pairs that aid surface redox reactions. 'Plasmonic photocatalysis' is a subset of photocatalysis, where localised surface plasmon resonance ('LSPR', typically visible light excitation) drives the DRM reaction, as opposed to bandgap excitation. 'Photothermal catalysis' occurs when heat generated by light drives the reaction. When the heating is insufficient to catalyse the reaction, a thermal

input may also be added ('photothermally driven'). The current review concentrates on a subset of photothermally driven catalysis, herein called 'visible light-assisted' thermocatalysis, which combines heating with visible light illumination (*i.e.*, no bandgap excitation). The role of bandgap excitation is not considered as recent reviews detailed the role of bandgap excitation and LSPR/bandgap excitation coupling for photocatalytic DRM [9,10].

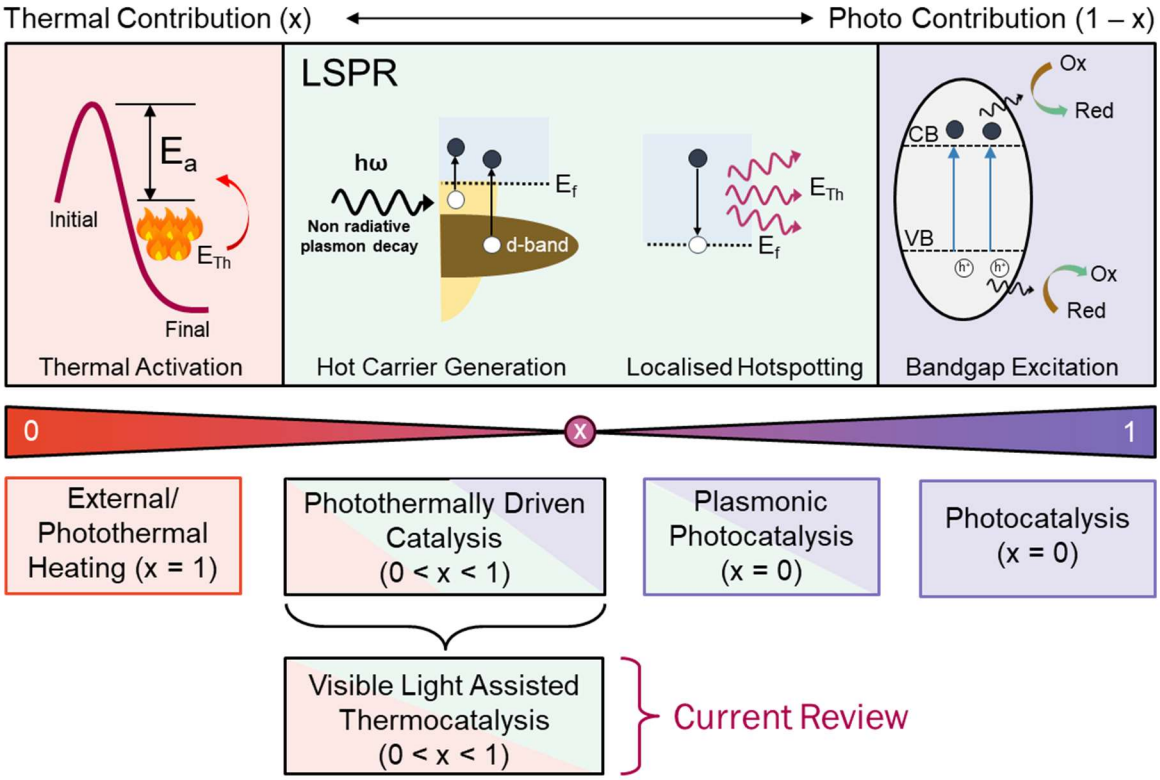

Figure 7. Establishing the mechanisms and definitions for the various solar-illumination avenues. The relative contribution of thermochemistry is given by x (x = 1 indicates thermocatalysis). The driving forces behind the photothermal catalytic DRM are thermal activation, hot carrier generation, localised hotspotting and bandgap excitation. The current review examines 'visible light-assisted' thermocatalysis, a thermal/LSPR hybrid approach classified under 'photothermally driven catalysis'.

4.1. Physics of Localised Surface Plasmon Resonance

4.1.1. Visible Light Absorption Mechanism

The LSPR effect occurs when a metal (smaller than the wavelength of the incident light) is illuminated. This invokes oscillation of the metal's free electrons within the light wave's alternating polarity (Figure 8a) [106,107]. The particle's electron cloud displacement by its attraction to the EMR wave resists the restoring force from the particle's nucleus, forming a dipole moment about the particle (Figure 8b). The absorption properties of the dipole moment accentuate the capture of the EMR's energy [108–112]. The oscillation frequency of a particle's electrons will increase until it stabilises at a frequency known as the 'plasmonic frequency', matching the frequency of the EMR wave. With sufficient energy, an outer d-shell electron of the absorber material may reach an excited state. Here, the electron is considered as a 'hot electron' (or 'hot-carrier'), which has sufficient energy to overcome the Schottky barrier of the metal oxide support, or the electron decays from this excited state and releases the absorbed energy as heat that raises the local temperature (known as 'localised hotspotting').

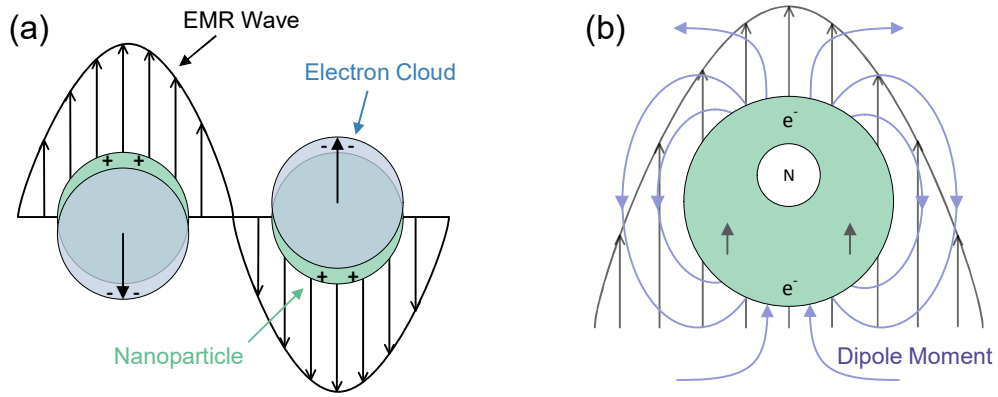

Figure 8. (**a**) Electron cloud movement stimulates oscillation within the incident EMR. (**b**) Creation of the dipole moment about the particle as a result of oscillation. Image (**a**) adapted with permission from Rodrigues et al. [107]. CC BY. (**b**) Image adapted with permission from Bora et al. [112]. CC 3.0.

4.1.2. LSPR-Induced Effects in DRM

The hot-carrier may directly aid the DRM by altering the surface charge of the active metal and, in some situations, the support material. Hot-carrier generation occurs instantaneously (<100 fs), where the energy from the absorbed EMR raises the electron's energy state beyond its Fermi level [106]. On the active metal, these electrons can induce a surface charge transfer, changing the local basicity of the active metal and facilitating the adsorption and conversion of the reaction intermediates [106,113,114].

Alternatively, the hot electrons may migrate across the Schottky junction (the interface between the active metal and metal-oxide support) when the support has semiconductor properties [106,115,116]. The hot carrier can then relocate to the support surface, facilitating CO_2 activation or CO_2 reduction and carbonate intermediate formation via surface charge transfer (Figure 9) [105,106]. The LSPR phenomenon distinguishes itself from other photoexcitation methods as the electron is not in thermal equilibrium with the catalyst, so the high electron energy aids its transition to the support material [116]. The hot electron can assist in catalysing the reaction by lowering the activation energy of one or several reaction intermediates, directly improving the kinetics [106].

Alternatively, the hot electron may also decay to its Fermi level, releasing the supplementary energy as heat in a process called 'relaxation' (Figure 9) [106]. The heat raises the local surface temperature of the active metal, known as 'localised hotspotting'. The increased local temperature may facilitate bond breaking or surface adsorption, improving the conversion rate of the DRM reaction intermediates, especially as DRM is endothermic [111,117–119].

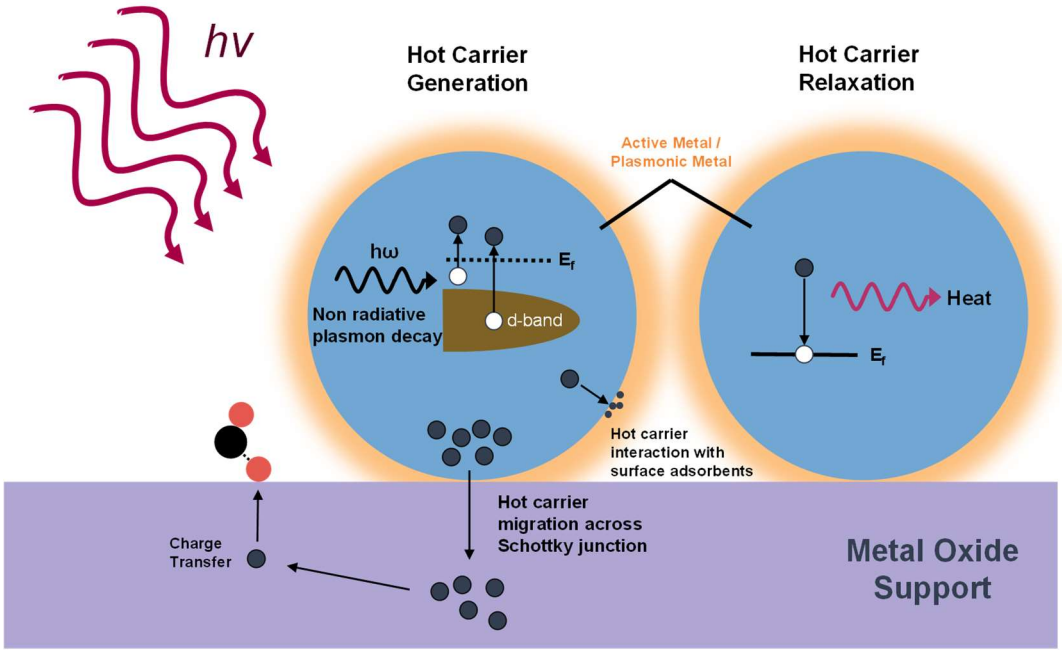

Figure 9. Hot carrier generation and relaxation occur upon the visible light illumination of a metal/metal oxide catalyst, as described by Ghoussoub et al. [106]. The dark blue circles denote electrons, and the white circles denote electron holes.

4.1.3. Decoupling Relative Contributions

Distinguishing between the direct contribution of hot carriers and localised hotspotting is challenging, which limits the understanding of the role of visible light illumination in enhancing DRM. Several authors employed scanning electrochemical microscopy (SECM) and similar methods to quantify the hot electrons upon visible light illumination [120–123]. SECM separates the relative contributions of hot electrons and localised hotspotting, although it is not performed in the context of a reaction. The hot electrons may be used directly in the reaction context, and the heat energy from the localised hotspotting may be transferred to instantaneous reaction intermediates or products. This complicated LSPR pathway remains elusive, and a better understanding is paramount to designing a light-receptive catalyst.

4.2. Influence of Process Variables

4.2.1. Material Selection

The influence of the LSPR phenomenon in the DRM depends strongly on material selection. Selected metals, known as 'plasmonic metals', have a narrow plasmonic response at specific EMR wavelengths, defined by their absorption spectra (Figure 10) [26]. LSPR may be integrated into the DRM by combining a plasmonic metal such as gold (Au), silver (Ag) or copper (Cu) with thermocatalytically active metals, forming a bimetallic catalyst and illuminating the catalyst with the characteristic LSPR wavelength of the plasmonic material [26,124,125].

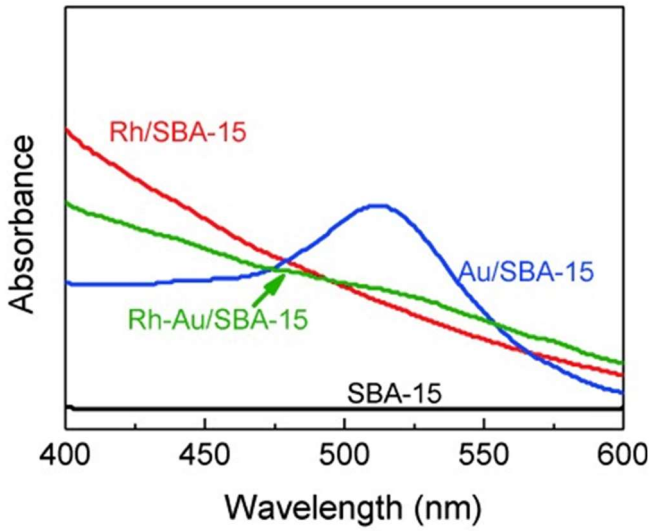

Figure 10. UV-vis absorption spectra of monometallic Rh (red) and Au (blue) on SBA-15 (mesoporous silica) and bimetallic Rh-Au (green) on SBA-15. The neat SBA-15 support (black) had negligible UV-vis absorption. The sharp Au peak at ~ 520 nm suggests single wavelength enhancement would induce a strong light response, whereas broad Rh/SBA-15 suggests the full visible light spectrum is more suitable. Image adapted with permission from Liu et al. [26]. Copyright © 2015, John Wiley and Sons.

Alternatively, metals smaller than the wavelength of incident light that has a high concentration of free carriers may exhibit surface plasmon effects [126]. Transitional metals like Ni or Co have a lower free carrier concentration than 'traditional' plasmonic metals, leading to a dampened LSPR response [126,127]. However, the interband and intraband transitions of Ni and Co produce broader visible light absorption than the wavelength-specific response of plasmonic materials [126,127]. As such, stimulating a conventional, transitional metal catalyst (Ni or Co) using a broad visible light spectrum has achieved comparable results to incorporating plasmonic metals [55,85,128].

4.2.2. Thermal Effects

For many reactions, the plasmonic contribution alone cannot provide enough energy to catalyse the DRM. Consequently, a combination of plasmonic-catalysis and thermocatalysis is required. For the endothermic DRM reaction, the local temperature increase provided by radiative plasmon decay, coupled with the hot electron contribution, may drive the forward reaction by improving the activation of CH_4 and stimulating enhanced surface charge transfer that assists with converting adsorbates [106,113,114].

Decoupling the thermal and non-thermal contributions to the reaction is challenging [129]. Currently, reaction rate modelling is employed to determine the thermal reaction rate, which is compared to the overall reaction rate to determine

the respective non-thermal contribution. Other techniques, such as *in-situ* DRIFTS and DFT modelling, compare the surface-adsorbed intermediates of thermal and light-assisted reaction conditions to distinguish changes in the reaction mechanism upon illumination [28,31,85]. The experimental and theoretical models overlook the symbiotic relationship between thermal and light effects. As the temperature increases, more energy is supplied to the surface electrons, reducing the required energy for excitation, which improves the LSPR response [130].

5. Light-Assisted DRM

Since the early conception of LSPR-incorporated DRM in 2015 by Liu et al., many mechanistic studies have been conducted on various materials [26]. This section will first introduce the techniques employed to obtain insights into the DRM mechanism under light before assessing the progression of catalyst design for light-assisted DRM. Early approaches for integrating visible light into DRM focused on incorporating plasmonic materials like Ag, Au and Cu into traditional thermocatalysts [20]. Light-assisted DRM then targeted the plasmonic response of non-noble metals known to be DRM-active. As outlined in Section 4, it is crucial to note that all metals smaller than the wavelength of the incident light will all metals exhibit a plasmonic response [131]. Noble metals are often characterised by broad visible light absorption, as opposed to the more focused wavelengths demonstrated by plasmonic metals. As these noble metals are still limited by their high cost, current literature focuses on using non-noble metals like Ni and Co for light-assisted DRM.

5.1. Probing the Light-Assisted Reaction Mechanism

Literature typically probes the light-assisted reaction conditions through techniques such as *in-situ* DRIFTS, isotopic experiments and DFT calculations. *In-situ* DRIFTS measures the diffuse scattering of an incident infrared (IR) beam striking the powdered catalyst sample. The incident IR excites molecules on the catalyst surface, stimulating vibrations that cause changes in the molecule's dipole moment [132]. The excitation wavelength is characteristic of the surface-adsorbed species, allowing the direct identification of species adsorbed onto the catalyst's surface. Measuring the transient response upon inducing small changes to the reaction (e.g., temperature step or chemical pulse) indicates which species are involved in the reaction mechanism [132]. Light illumination typically occurs using a focused laser [133,134] or Xe lamp [55,85] light source through a separate window to the IR beam path. For light-assisted DRM, *in-situ* DRIFTS can compare the reaction intermediates under thermal and light-assisted DRM conditions. Of particular interest is the presence of the methoxy species (CH_xO, x = 1–3), which indicates that CH_x is oxidised before complete dehydrogenation, preventing carbon formulation through CH_4 cracking [55,85,134]. While the technique effectively identifies the reaction intermediates, *in-situ* DRIFTS spectra are often highly convoluted, making quantitative assessments challenging [132]. Furthermore, the signal intensity attenuates as the temperature increases, limiting the assessment to a low-temperature DRM range (typically <700 °C) [132,134].

Isotopic labelling is a powerful tool to probe the light-assisted DRM mechanism. Isotopes are created by adding neutrons to elements, creating elemental tracers that aid the deconvolution of the reaction mechanism. Isotopic labelling is effective at determining the origin of certain species and is often coupled with *in-situ* DRIFTS to provide a more comprehensive understanding of the reaction mechanism. Isotopically labelling C species in either CO_2 ($^{13}CO_2$) or CH_4 ($^{13}CH_4$) may provide insight into the origins of certain products, as well as carbon formation, whereby the spent carbon may be gasified to produce either ^{12}CO or ^{13}CO, depending on the labelling of CO_2 or CH_4 [85,135]. The involvement of labile oxygen species may be determined by reducing the catalyst surface and oxidising with isotopically labelled O (^{18}O) before the reaction. If the catalyst's labile O are actively involved in the reaction mechanism, a $C^{18}O$ product would be evident [63,135]. The products are measured with a mass spectrometer, distinguishing the molecules by molecular weight. Coupling isotopic labelling with *in-situ* DRIFTS causes a shift in the molecule's fingerprint, providing a better distinction between active reaction intermediates and spectator species [85,135].

Density functional theory calculations provide a theoretical understanding of the reaction mechanism by providing insight into the adsorption energy of reaction intermediates, the reaction energies of key elementary reactions, as well as the preferred binding sites. The complexity of the reaction limits the scope of the DFT calculations. For light-assisted DRM, the role of light in CH_4 dissociation has been investigated by modelling a slab of active metal [135,136]. No support is present in the model, as the model assumes for deposits of significant size, the CH_4 dissociation reaction will take place on the active metal without the influence of the support. Similarly, the CH_4 dissociation model does not account for the adsorption and disassociation of CO_2. The role of light is assessed by changing the excitation states of the active metal, mimicking the role of hot electrons in the reaction mechanism [28,136]. Similarly, work by Zhu et al.

added additional electrons to replicate the role of hot carriers [137]. The CO_2 dissociation reaction has also been investigated following the same strategy as the CH_4 dissociation reaction using models of the active metal, an active metal atom on the support and a slab of support [28,136]. The reliability of these techniques to model light using DFT must be questioned, as the narrow system bounds may not be fully representative of reaction conditions.

5.2. Early Approaches to Light-Assisted DRM

Initial light-assisted DRM strategies incorporated plasmonic metals such as Ag [138], Au [26,27,139] and Cu [28] into known thermally active catalysts. Liu et al. studied the influence of Au on a Pd-Au/Al_2O_3 catalyst [139]. Pd/Al_2O_3 was the most active material, but low Au content (90Pd-10Au/Al_2O_3) had similar catalytic performance to the Pd/Al_2O_3 once illuminated, indicating that LSPR supplemented the activity lost from Au doping. Au/Al_2O_3 demonstrated negligible conversion, suggesting that Au was DRM inactive.

Song et al. employed a Pt-Au/SiO_2 catalyst with limited active metal loading (0.5 wt% Pt and 1.0 wt% Au) [27]. The combination resulted in a ~25% increase in CO_2 conversion relative to the thermal Pt-Au/SiO_2 when illuminating at the plasmonic wavelength range of Au ($480 < \lambda < 600$ nm; Figure 11a,b) [27]. While light illumination considerably improved the product generation, no significant change in the H_2/CO ratio was observed, suggesting that light accelerated the DRM reaction but did not alter the reaction pathway. The authors used finite-difference time-domain (FDTD) simulations to demonstrate that the generation of hot electrons from Pt and Au likely drove the conversion of adsorbates, improving reaction rates. The influence of light on catalytic stability was not investigated in this work [27]. *In-situ* DRIFTS and DFT analysis demonstrated reduced $HCOO_{ads}$ and CO_{ads} concentrations upon illumination. The authors postulated that the lower surface coverage upon illumination meant the CO and H_2 species were more likely to desorb, increasing activity [27]. While the authors demonstrated the potential of light for activity improvements, they did not assess catalyst stability.

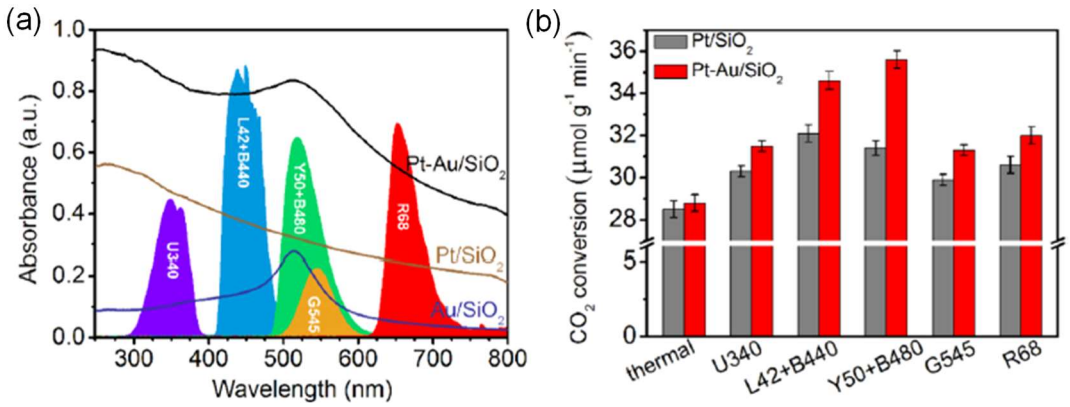

Figure 11. (**a**) UV-vis absorption spectra of Pt/SiO_2 (brown), Pt-Au/SiO_2 (black) and Au/SiO_2 (blue), overlaid with light source emissions with various filters (purple—U340, blue—L42+B440, green—Y50+B480, gold—G545 and red—R68). (**b**) CO_2 conversion for Pt/SiO_2 (grey) and Pt-Au/SiO_2 (red) under various filters for light-assisted DRM. T = 673 K, I_v = 0.6 W cm^{-2}. Image adapted with permission from Song et al. [27]. Copyright © 2018, American Chemical Society.

Zhou et al. showed the effectiveness of a Ru_x-$Cu_{(2-x)}$/MgO-Al_2O_3 ($0 < Ru < 0.5$ wt%) catalyst under visible light illumination [28]. The 20Cu/MgO-Al_2O_3 could not catalyse the DRM reaction, instead promoting the undesirable RWGS reaction to favour CO production. Under a 19.2 W·cm^{-2} light intensity ($400 < \lambda < 800$ nm), the authors demonstrated a seven-fold increase in the reaction rate at 727 °C. The H_2/CO ratio increased from ~0.2 to 1.0, suggesting that the reaction was more selective to DRM than RWGS under illuminated conditions. DFT modelling indicated that light illumination resulted in a mechanistic change. Under thermal conditions, adsorbed H and O species coupled, forming OH_{ads} and eventually water (*i.e.*, RWGS reaction). The OH_{ads} formation limited the availability of oxygen to oxidise the surface carbon formed by CH_4 disassociation, resulting in carbon accumulation and catalyst deactivation. The authors suggested that the role of localised hotspotting was negligible at high operating temperatures (~1000 K), so Cu-generated hot carriers-promoted the associative desorption of H_2 by electronic transitions under light-assisted reaction conditions. (Figure 12a,b). The rapid coupling of H_{ads} to form H_2 prevented OH_{ads} formation, thereby increasing the availability of O_{ads} to gasify the surface carbon (Figure 12c). In addition to the activity enhancements, illuminating the catalysts with visible light achieved significant selectivity and stability improvements [28]. The extent of catalytic improvement may partly be attributed to the endothermicity of the reaction, whereby the additional energy through

LSPR incorporation drove the forward DRM reaction [106,113,114].

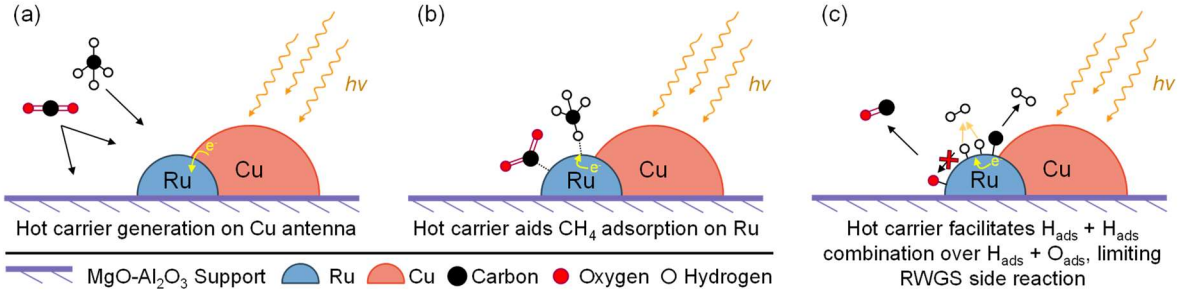

Figure 12. Summary of a study by Zhou et al. that suggests light's role in the DRM mechanism over Ru_x-$Cu_{(2-x)}$/MgO-Al_2O_3 catalysts [28]. (**a**) Light was adsorbed onto the Cu antenna, facilitating hot carrier generation and migration to the Ru reactor site. (**b**) Hot carrier aided the adsorption and disassociation of CH_4 on the Ru reactor site. (**c**) Hot carriers facilitated the coupling of H_{ads}, preventing the combination of H_{ads} and O_{ads} to form OH_{ads}, the precursor to water generation (*i.e.*, RWGS side reaction), leading to improved stability (better oxygen availability) and selectivity.

5.3. Light-Assisted DRM on Non-Noble Catalysts

As plasmonic metals such as Au, Ag and Cu are not DRM active or selective and noble metals are limited by their high cost, more recent work has focused on illuminating the broad-spectrum absorbance of non-noble DRM catalysts (*i.e.*, Ni or Co as the active metal) [25,140–142]. Liu et al. observed the interaction between active metal loading and light impact for Ni/Al_2O_3 catalysts (T_R = 550 °C, I_v = 1.07 W·cm^{-2}) [25]. The $10Ni/Al_2O_3$ showed the most significant light enhancement (compared to 5, 15 and 20 wt% Ni) despite $15Ni/Al_2O_3$ being the most active. The authors demonstrated that illuminating Al_2O_3 and SiO_2-supported Ni had similar impacts on catalyst performance, leading to the belief that Ni drove the light enhancement. They attributed the 10 wt% Ni illuminated performance to greater visible light absorption, but the authors did not address why the intensity of light absorption peaked at 10 wt% Ni and then decreased significantly by 20 wt% Ni.

Hu et al. studied Al_2O_3 cluster-modified Ni/Al_2O_3 ('ACM', clusters deposited onto Ni) under light [143]. The Ni/Al_2O_3 reference deposited carbon upon illumination, whereas ACM-Ni/Al_2O_3 improved carbon resistance by an order of magnitude. The authors used DFT to show that surface modification with alumina clusters improved the oxidation of C_{ads} and increased the enthalpy of C_{ads} polymerisation under light, resulting in improved catalyst stability and yielding better H_2 and CO generation rates upon illumination (2.9 and 1.9 times greater than thermal conditions, respectively). The authors did not investigate the impact of light on carbon formation or attribute the enhancement to specific properties of the Al_2O_3 clusters [143].

Liu et al. studied the influence of Ni size for light-assisted DRM over Ni/Al_2O_3. Deposits below 17.3 nm in diameter were required to achieve light-enhanced activity for their system [140]. Above 17.3 nm, the Ni catalysts had a low conversion with minor light enhancement (I_v = 1.07 W·cm^{-2}, 300 < λ < 800 nm). Below this threshold, the 3 nm deposit possessed the best activity and light enhancement, whereas the 9.5 and 10.1 nm catalysts had similar activity (attributed to 5 and 10 wt% Ni, respectively), indicating that the smaller particles lead to greater conversions under visible light. The origin of inactivity for deposits greater than 17.3 nm was not studied, which could be addressed with a systematic deposit size mechanistic study. Similarly, catalyst deactivation was evident for greater loadings, which was not investigated in the work.

Using light conditions akin to their previous studies, Liu et al. observed the influence of morphology on light-assisted DRM by synthesising impregnated Ni/SiO_2, $Ni@SiO_2$ core-shell structure and $Ni@SiO_2$ yolk-shell structure [75]. Under thermal conditions, the catalysts followed the order Ni/SiO_2-Im > $Ni@SiO_2$-yolk > $Ni@SiO_2$-core, which was inversely related to the Ni deposit size. The impregnated catalyst had the greatest CH_4 and CO_2 activity enhancement under light, though it deactivated rapidly due to carbon formation. The authors used *in-situ* electron spin resonance spectroscopy to identify oxygen radicals under reaction conditions (CO_2/CH_4 = 1, T = 550 °C), suggesting that LSPR-generated hot carriers aided CO_2 disassociation. Comparable thermal gravimetric analysis and spent Raman spectroscopy profiles indicated no light-driven change in carbon amount or type for the impregnated catalyst. Conversely, both the yolk and core-shell structures were more stable upon illumination, as light facilitated the formation of active carbon over graphitic carbon. The authors did not associate the change in carbon type between the impregnated and shell-structured catalysts with any property of the support. Despite these changes in carbon type and stability, the

catalyst selectivities were analogous (H_2/CO ratio of 0.87 ± 0.04) and underwent negligible change upon illumination (<5% change, thermal basis). The comparability in the product selectivities suggests similar reaction mechanisms between the catalysts and under both thermal and light-assisted reaction conditions [75].

Recently, Zhang et al. studied bimetallic Ni_x-$Co_{1.5-x}/SiO_2$ catalysts (1.5 wt% metal loading) for photothermal DRM [55]. They found that Co had a strong interaction with SiO_2 and was inactive under thermal and illuminated conditions despite numerous thermocatalytic (Section 3.2) and photocatalytic [144–146] studies reporting comparable Ni and Co activity (Figure 13a). Under light, Ni/SiO_2 reaction intermediates remained the same, indicating no change in the reaction mechanism. The authors attributed the better performance to purely localised hotspotting. For $Ni_{1.2}$-$Co_{0.3}/SiO_2$, the CHO_{ads} concentration increased upon illumination, indicating that a small Co presence led to the light-promoted oxidation of CH_{ads} (Figure 13b). The authors used transmission electron microscopy, thermal gravimetric analysis and Raman spectroscopy to demonstrate that no carbon was evident for $Ni_{1.2}$-$Co_{0.3}/SiO_2$, indicating that light promoted a stable reaction pathway. Despite the lack of carbon, $Ni_{1.2}$-$Co_{0.3}/SiO_2$ deactivated by ~20% (CO_2 conversion) after 30 h, which the authors attributed to active metal sintering. Zhang et al. did not investigate or discuss the stability of the other catalysts in their study [55].

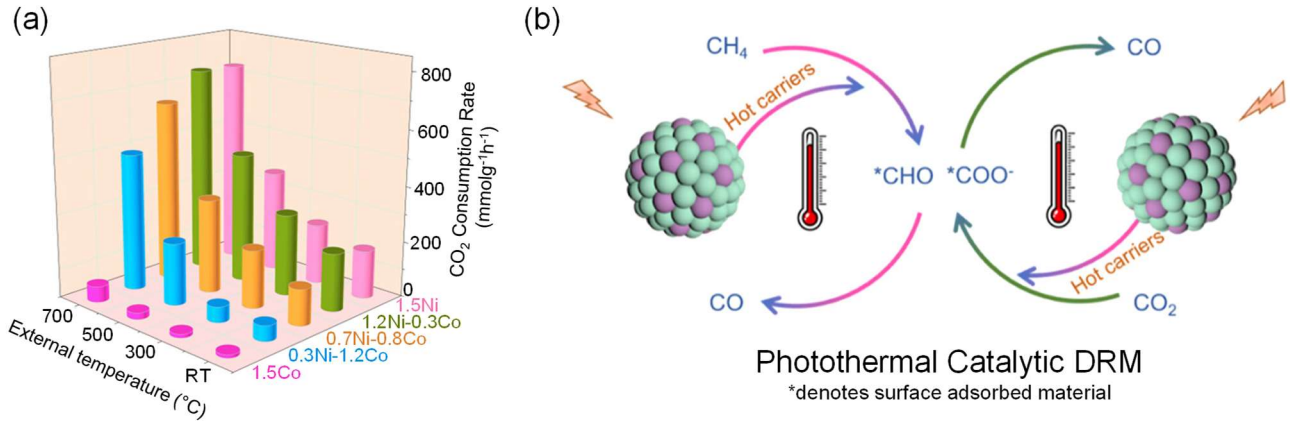

Figure 13. (**a**) Photothermal DRM performance over Ni_x-$Co_{1.5-x}/SiO_2$ catalysts, T = 700 °C, CO_2/CH_4 = 1, flow = 20 mL·min^{-1}, I_V = 9 W·cm^{-2}. Co/SiO_2 had negligible activity, but the bimetallic effect of Ni–Co demonstrated superior performance for 1.2 wt% Ni, 0.3 wt% Co. (**b**) Proposed photothermal catalytic DRM mechanism, suggesting that the hot carriers generated through LSPR aided both the oxidation of CH to form CHO and the adsorption of CO_2. Image adapted with permission from Zhang et al. [55]. Copyright © 2023, Royal Society of Chemistry.

While Liu et al. demonstrated the similarity of inactive supports, Zhang et al. first highlighted the potential of an active support for photocatalytic DRM (no additional external heating, I_v = 0.1 W·cm^{-2}, λ > 420 nm) [135]. The authors showed that the rate of carbon deposition of illuminated Ni/CeO_2 (0.0125 $g_c \cdot g_{cat}^{-1} \cdot h^{-1}$) was considerably less than Ni/SiO_2 (0.23 $g_c \cdot g_{cat}^{-1} \cdot h^{-1}$). The authors identified isotopic $C^{18}O_2$ tracing coupled with *in-situ* DRIFTS uncovered CO_2 turnover on the ceria SOVs stimulated reverse oxygen spillover (O disassociated from CO_2 migrates to Ni), resulting in reaction with $CH_{x,ads}$ that formed the more stable CH_xO intermediate. DFT results confirmed that activity improvements stemmed from reduced CH_4 disassociation energy on Ni [135]. Du et al. synthesised a Ni/CeO_2-ZrO_2 catalyst, which, while offering a small activity improvement, exhibited significantly greater stability under light [147]. They suggested that light facilitated the release of SOV-trapped O atoms to gasify surface carbon in a similar manner to the Ru_x-$Cu_{(2-x)}/MgO$-Al_2O_3 study by Zhao et al. [28]. While the experiment employed *in-situ* DRIFTS, there was no direct evidence verifying the role of trapped oxygen in C_{ads} oxidation. The nature of the surface carbon on the Ni/CeO_2 and Ni/ZrO_2 was not studied.

Lorber et al. studied the optical properties of Ni/CeO_{2-x} nanorods using *in-situ* UV-vis. Under light, CO_2 and CH_4 reaction rates increased 8-fold [31]. The CeO_2 bandgap shifted into the visible light spectrum after reduction at 450 °C for 30 min, which stimulated photoexcited electron transfer from the Ce conduction band to the Ni under light-assisted reaction conditions (Figure 14a). The authors showed that the RWGS reaction was not promoted by light. They postulated that as CO_2 disassociation is the rate-limiting step for RWGS, the visible light likely did not influence CO_2 adsorption onto CeO_2, which is thermally driven at 400 °C. Rather, the visible light promoted CH_x disassociation on the surface Ni through the accumulated photo-excited electrons on Ni (Figure 14b), which supports the DFT results of Zhang, Mao et al. [135]. This postulation was directly evidenced by an 8.5-fold increase in the CH_4 conversion rate

upon illumination, coupled with an improved H_2 yield that increased the H_2/CO ratio from 0.23 under thermal conditions to 0.59 under light [31]. This increase in selectivity aligns with observations from Zhou et al. and Hu et al. [28,143].

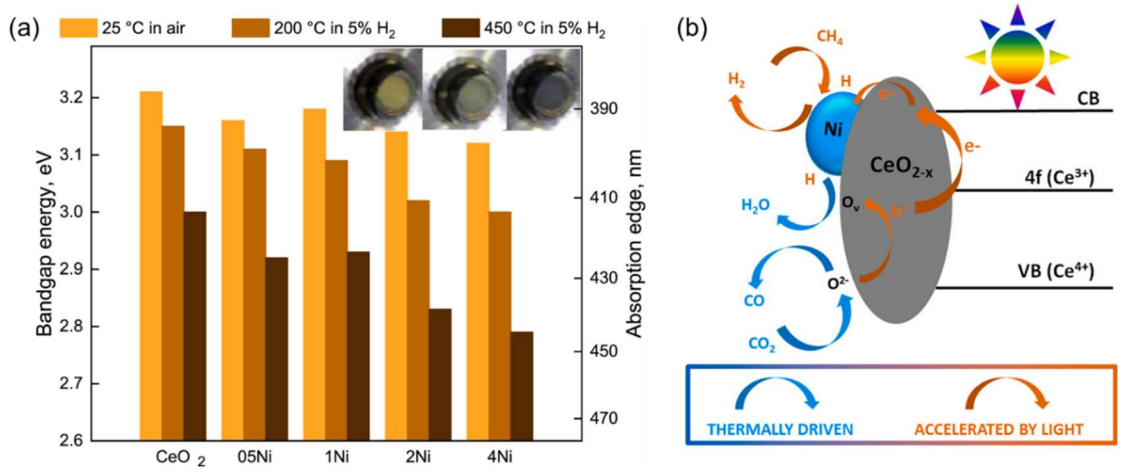

Figure 14. (**a**) Influence of Ni loading and reduction conditions on the bandgap energy and adsorption edge for Ni/CeO_{2-x} nanorods. (**b**) Proposed visible light-assisted DRM mechanism. Image adapted with permission from Lorber et al. [31]. CC 4.0.

Recent work by our group assessed the role of visible light illumination on CH_x oxidation rate by synthesising Co/xCeO_2-Al_2O_3 (x = 0–20 mol% Ce) catalysts [134]. While incorporating a low Ce content (~5 mol%) improved the thermocatalytic DRM stability, all catalysts deactivated upon illumination with visible light (white LED, $420 < \lambda < 710$ nm, $I_V = 2.0$ W·cm^{-2}), despite an increase in basicity with Ce content. Characterisation of the spent catalysts identified that the carbon transitioned from a more stable amorphous carbon to whisker carbon (β and v-type, respectively, in Figure 3). Light accelerated the decomposition of CH_4, causing an imbalance between the CH_x (x = 0–3) oxidation and carbon deposition rates, resulting in catalyst deactivation (Figure 15). No CH_xO intermediate was identified by *in-situ* DRIFTS under thermal or visible light-assisted reaction conditions, suggesting that the CH_x oxidation rate limited the system.

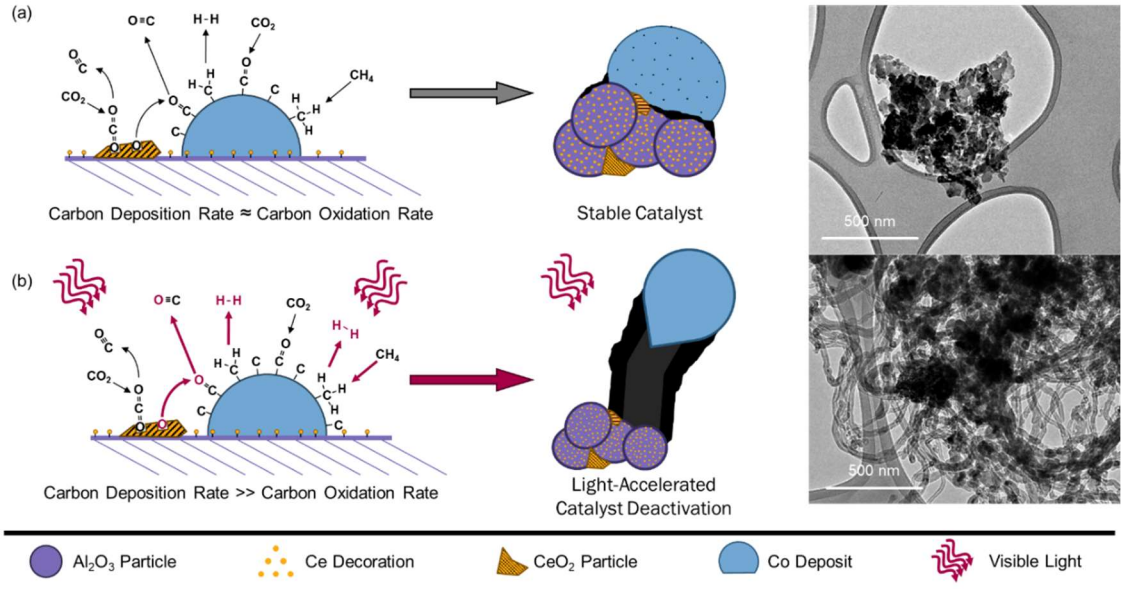

Figure 15. Light-assisted DRM reaction scheme over Co/xCeO_2-Al_2O_3. (**a**) Thermal DRM; oxygen trapped in ceria's oxygen vacancies could oxidise surface carbon, preventing carbon accumulation. (**b**) Visible light-assisted DRM; light accelerated CH_4 dehydrogenation, outbalancing the support's oxidative capacity, resulting in complete CH_4 cracking. The carbon deposition rate exceeded the carbon oxidation rate, causing light-accelerated catalyst deactivation. Image adapted with permission from O'Connell et al. [134]. Copyright © 2024, Royal Society of Chemistry.

There have been an array of published studies in the light-assisted DRM field that consider various key aspects of catalyst design, including the influence of active metal selection, size and loading, as well as the support selection and the impacts of morphology and basicity on light-assisted DRM performance. A summary of the catalytic activity and key takeaways for the various light-assisted DRM catalysts considered in this review is provided in Table 2.

Table 2. Summary of light-assisted methane dry reforming studies.

Catalyst	Reaction Conditions	Light Conditions	Conversion Rates	Highlights & Additional Comments	Ref.
xNi/Al_2O_3	m_{cat} = 50 mg T = 550 °C CH_4/CO_2 = 1/1 Flow rate: 20 mL·min^{-1}	Xe Lamp, HA30 filter I_v = 1.1 W·cm^{-2} 300 < λ < 800 nm	$10Ni/Al_2O_3$ H_2 Yield (Th) = 65 μmol·g^{-1}·min^{-1} H_2 Yield (VL) = 126 μmol·g^{-1}·min^{-1} CO Yield (Th) = 70 μmol·g^{-1}·min^{-1} CO Yield (VL) = 129 μmol·g^{-1}·min^{-1}	Comparable performance with Ni/SiO_2 control indicates that light-assisted DRM is driven more by the active metal than support selection.	[25]
Rh-Au/ SBA-15	m_{cat} = 5 mg T = 500 °C CH_4/CO_2 = 1/1 Flow rate: 20 mL·min^{-1}	Xe Lamp, L42 + HA30 filter I_v = 0.31 W·cm^{-2} Visible light (λ = n.s. †)	H_2 Yield (Th) = 59 μmol·g^{-1}·min^{-1} H_2 Yield (VL) = 113 μmol·g^{-1}·min^{-1} CO Yield (Th) = 69 μmol·g^{-1}·min^{-1} CO Yield (VL) = 109 μmol·g^{-1}·min^{-1}	Au was inactive relative to Rh, but the bimetallic catalyst exhibited the best light response.	[26]
$Pt-Au/SiO_2$	m_{cat} = 20 mg T = 400 °C CH_4/CO_2 = 1/1 Flow rate: 20 mL·min^{-1}	Xe Lamp, HA30 filter I_v = 0.6 W·cm^{-2} 300 < λ < 800 nm	H_2 Yield (Th) = 41 μmol·g^{-1}·min^{-1} H_2 Yield (VL) = 94 μmol·g^{-1}·min^{-1} CO Yield (Th) = 55 μmol·g^{-1}·min^{-1} CO Yield (VL) = 122 μmol·g^{-1}·min^{-1}	Au was inactive relative to Pt, but the bimetallic performed better than the Pt/SiO_2 control upon illumination. $Pt-Au/SiO_2$ adsorbed UV and visible light, but performance enhancement was attributed to the Pt/Au plasmonic response.	[27]
$Cu_{19.8}Ru_{0.2}/MgO-Al_2O_3$	m_{cat} = 1.5 mg T = 327–727 °C CH_4/CO_2 = 1/1 Flow rate: 16 mL·min^{-1}	Fiber Laser I_v = 19.2 W·cm^{-2} 400 < λ < 800 nm	CH_4 Rxn Rate (Th) = 1.0 μmol·g^{-1}·min^{-1} (VL) = 4.5 μmol·g^{-1}·min^{-1}	DFT showed that light promoted H_2 desorption, improving the availability of surface oxygen (otherwise forming water by RWGS) to gasify surface carbon.	[28]
$Pd_x-Au_{(1-x)}/Al_2O_3$	m_{cat} = 15 mg T = 500 °C CH_4/CO_2 = 1/1 Flow rate: 20 mL·min^{-1}	Xe Lamp, L42 + HA30 filter I_v = 19.2 W·cm^{-2} 400 < λ < 800 nm	$Pd_{90}Au_{10}/Al_2O_3$ X_{CH_4} (Th) = 771 μmol·g^{-1}·min^{-1} X_{CH_4} (VL) = 936 μmol·g^{-1}·min^{-1} X_{CO_2} (Th) = 1007 μmol·g^{-1}·min^{-1} X_{CO_2} (VL) = 1205 μmol·g^{-1}·min^{-1}	Au dampened Pd activity. Greatest light enhancement occurred for $Pd_{90}Au_{10}/Al_2O_3$. Pd deactivated significantly.	[139]
$4Ni/CeO_{2-x}$	m_{cat} = 2 mg T = 180–470 °C CH_4/CO_2 = 1/1 Flow rate: 20 mL·min^{-1}	LED I_v = 0.79 W·cm^{-2} 400 < λ < 700 nm	CH_4 Rxn Rate (Th, 470 °C) = 3 mmol·g^{-1}·min^{-1} (VL, 460 °C) = 4 mmol·g^{-1}·min^{-1} CO_2 Rxn Rate (Th, 470 °C) = 10.5 mmol·g^{-1}·min^{-1} (VL, 460 °C) = 10 mmol·g^{-1}·min^{-1}	In-situ UV-vis determined that the CeO_2 bandgap shifted from UV to visible light absorption region. Suggests CO_2 disassociation was thermally driven, but accumulated photo-excited electrons facilitated CHx disassociation on Ni.	[31]
$1.2Ni-0.3Co/ SiO_2$	m_{cat} = 30 mg T = 700 °C CH_4/CO_2 = 1/1 Flow rate: 20 mL·min^{-1}	300W Xe Lamp I_v = 9 W·cm^{-2} 400 < λ < 700 nm	H_2 Yield (Th) = 15 μmol·g^{-1}·min^{-1} H_2 Yield (VL) = 75 μmol·g^{-1}·min^{-1} CO Yield (Th) = 30 μmol·g^{-1}·min^{-1} CO Yield (VL) = 85 μmol·g^{-1}·min^{-1}	Relative to Ni, Co was inactive for DRM. Strong $Co-SiO_2$ interaction prevented Ni sintering at low Co loading (0.3 wt%). No change to the reaction intermediates upon illumination.	[55]
Ag-La/CNNT	m_{cat} = 150 mg T = 700 °C CH_4/CO_2 = 1/1 Flow rate: 5 mL·min^{-1}	Solar Simulator I_v = 0.1 W·cm^{-2} λ = n.s.†	H_2 Yield (VL) = 14.9 μmol·g^{-1}·min^{-1} CO Yield (VL) = 12.8 μmol·g^{-1}·min^{-1}	Ag-La synergy leads to effective interfacial carrier separation on protonated carbon nitride nanotubes.	[138]
xNi/Al_2O_3	m_{cat} = 50 mg T = 550 °C CH_4/CO_2 = 1/1 Flow rate: 20 mL·min^{-1}	Xe Lamp, HA30 filter I_v = 1.07 W·cm^{-2} 300 < λ < 800 nm	$1Ni/Al_2O_3$ H_2 Yield (Th) = 2.2 mmol·g^{-1}·min^{-1} H_2 Yield (VL) = 4.0 mmol·g^{-1}·min^{-1} CO Yield (Th) = 2.1 mmol·g^{-1}·min^{-1} CO Yield (VL) = 4.5 mmol·g^{-1}·min^{-1}	Wavelength-dependent performance indicated that the LSPR effect was prevalent for smaller Ni deposits, but interband transition dominated for larger Ni nanoparticles. $1Ni/Al_2O_3$ was most active under light.	[140]

Rh/Al_2O_3	m_{cat} = 300 mg T = 200 °C CH_4/CO_2 = 1/1 Flow rate: 20 mL·min^{-1}	Xe Lamp, Y-43 filter I_v = 0.19 W·cm^{-2} λ > 420 nm	H_2 Yield (Th) = 16.1 μmol·g^{-1}·min^{-1} H_2 Yield (VL) = 133 μmol·g^{-1}·min^{-1} CO Yield (Th) = 47.8 μmol·g^{-1}·min^{-1} CO Yield (VL) = 333 μmol·g^{-1}·min^{-1}	Larger Rh sizes resulted in greater surface temperature upon illumination, but catalytic activity decreased due to agglomeration. Despite lower thermal activity, Ni/Al_2O_3 control exhibited comparable light activity to Rh/Al_2O_3.	[141]
Ni/Al_2O_3	m_{cat} = 300 mg T = 300 °C CH_4/CO_2 = 1/1 Flow rate: 20 mL·min^{-1}	Xe Lamp, Y-43 filter I_v = 0.19 W·cm^{-2} λ > 420 nm	H_2 Yield (Th) = 35.5 μmol·g^{-1}·min^{-1} H_2 Yield (VL) = 123 μmol·g^{-1}·min^{-1} CO Yield (Th) = 62.8 μmol·g^{-1}·min^{-1} CO Yield (VL) =179 μmol·g^{-1}·min^{-1}	Of various transition metals (Fe, Ni, Cu, Zn, Rh, Pd, Ag, La, Pt and Au), only Ni, Rh and Pt exhibited a light response. Light performance changed with reduction temperature—metallic Ni was vital.	[142]
ACM-Ni/Al_2O_3	m_{cat} = 10 mg T = 602 °C CH_4/CO_2 ≈ 1/1 Flow rate: 90 mL·min^{-1}	500 W Xe Lamp I_v = 7.69 W·cm^{-2} λ > 420 nm	H_2 Yield (Th) = 22.3 μmolg^{-1}min^{-1} H_2 Yield (VL) = 40.7 μmolg^{-1}min^{-1} CO Yield (Th) = 65.6 μmolg-^{1}min^{-1} CO Yield (VL) =78.6 μmolg^{-1}min^{-1}	Alumina clusters deposited onto Ni/Al_2O_3 limited the Boudouard reaction, instead promoting the gasification of C_{ads}.	[143]
Ni/CeO_2	m_{cat} = 50 mg T = 807 °C CH_4/CO_2 ≈ 1/1 Flow rate: 122 mL·min^{-1}	Solar Simulator I_v = 0.1 W·cm^{-2} λ > 420 nm	H_2 Yield (VL) = 5.3 mmol·g^{-1}·min^{-1} CO Yield (VL) =6.3 mmol·g^{-1}·min^{-1}	Isotopic tracing of O identified that O turnover on ceria's SOVs promoted the formation of CH_xO intermediate, thereby preventing carbon formation from complete CH_x dehydrogenation.	[135]
Ni/CeO_2-ZrO_2	m_{cat} = 5 mg T = 700 °C CH_4/CO_2 ≈ 1/1 Flow rate: 1.5 mL·min^{-1}	Solar Simulator I_v = 0.3 W·cm^{-2} 300 < λ < 800 nm	H_2 Yield (Th) = 1.01 mmol·g^{-1}·min^{-1} H_2 Yield (VL) = 1.27 μmol·g^{-1}·min^{-1} CO Yield (Th) = 1.00 μmol·g^{-1}·min^{-1} CO Yield (VL) =1.14 μmol·g^{-1}·min^{-1}	Small activity improvement but considerable stability improvement. Suggested that O released from SOVs gasified surface carbon. Incorporation of ZrO_2 improved O availability.	[147]
Ni/CeO_2 (Atomic, Ni-O Coordinated)	m_{cat} = 25 mg T = 470 °C CH_4/CO_2 ≈ 1/1 Flow rate: 10 mL·min^{-1}	300 W Xe Lamp I_v = 2.4 W·cm^{-2} 320 < λ < 800 nm	H_2 Yield (Th) = 1.7 mol·mol$_{Ni}^{-1}$·min^{-1} H_2 Yield (VL) = 8.6 mol·mol$_{Ni}^{-1}$·min^{-1} CO Yield (Th) = 3.3 mol·mol$_{Ni}^{-1}$·min^{-1} CO Yield (VL) =7.6 mol·mol$_{Ni}^{-1}$·min^{-1}	SSITKA-DRIFTS showed that Ni-Ni coordination prompted CH_4 cracking under light, but Ni-O coordination (atomic Ni) suppressed carbon due to the preferential oxidation of CH_x over dehydrogenation.	[85]
Co/CeO_2-Al_2O_3 (10mol% Ce)	m_{cat} = 50 mg T = 650 °C CH_4/CO_2 ≈ 1/1 Flow rate: 24 mL·min^{-1}	White LED I_v = 2.0 W·cm^{-2} 420 < λ < 710 nm	H_2 Yield (Th) = 0.57 mmol·g^{-1}·min^{-1} H_2 Yield (VL) = 0.78 mmol·g^{-1}·min^{-1} CO Yield (Th) = 1.29 mmol·g^{-1}·min^{-1} CO Yield (VL) = 1.51 mmol·g^{-1}·min^{-1}	Incorporating CeO_2 into Al_2O_3 improved stability under thermal conditions but deactivated under light. Light-accelerated CH_x dehydrogenation rate outbalanced CH_x oxidation rate, resulting in catalyst deactivation by whisker carbon.	[134]
Ni/SiO_2 $Ni@SiO_2$-Yolk $Ni@SiO_2$-Core	m_{cat} = 50 mg T = 550 °C CH_4/CO_2 ≈ 1/1 Flow rate: 20 mL·min^{-1}	300 W Xe Lamp I_v = 1.07 W·cm^{-2} 300 < λ < 800 nm	$Ni@SiO_2$-Yolk H_2 Yield (Th) = 0.48 mmol·g^{-1}·min^{-1} H_2 Yield (VL) = 0.72 mmol·g^{-1}·min^{-1} CO Yield (Th) = 0.49 mmol·g^{-1}·min^{-1} CO Yield (VL) = 0.67 mmol·g^{-1}·min^{-1}	The impregnated Ni/SiO_2 was the most active but deactivated rapidly. $Ni@SiO_2$-Yolk and $Ni@SiO_2$-Core exhibited superior stability due to forming active carbon over graphitic carbon.	[75]

† n.s. = not specified.

6. Summary and Outlook

The DRM is a promising CO_2 utilisation solution that may ease the global energy transition to fossil-fuel alternatives. Currently, the significant thermal energy demand and competing side reactions, such as the reverse water gas shift and carbon deposition reactions like the Boudouard and CH_4 cracking, limit the DRM reaction. Common thermocatalysts such as metal oxide-supported Ni and Co often deactivate due to carbon deposition or active metal sintering at high operating temperatures, making catalyst stability crucial to DRM performance.

Inducing the LSPR mechanism by illuminating the catalyst with visible light may provide a unique opportunity to enhance the DRM stability while offsetting thermal energy requirements and help to overcome the limitations of the DRM. Achieving this outcome requires a comprehensive understanding of the catalytic systems and mechanisms behind supplementing the DRM reaction with visible light. The active metal selection has been briefly studied for light-assisted DRM, where several authors have demonstrated that illuminating conventional monometallic catalysts or incorporating a plasmonic metal to form a bimetallic catalyst effectively enhances catalytic activity and stability. Metals such as Ni, Pt, Pd, Ru, Rh, Co, Cu and Au have been studied independently, however no systematic study has determined which active metal combination is optimum for the DRM reaction. Several studies investigated active metal properties for light-assisted DRM, such as deposit size and loading, although all investigations were inconclusive in attributing the observed trends to physicochemical properties.

The studies assessed in this review highlighted light's potential to improve the catalytic activity of DRM. In particular, several studies reported that light boosted CH_4 conversion, improving the H_2 yield. In these studies, the H_2/CO ratio increased relative to thermal reaction conditions due to the enhanced availability of adsorbed hydrogen atoms under light that promoted the preferential reaction of H_{ads} to form H_2 over the combination with O_{ads} to form OH_{ads}, a key reaction step in the RWGS side reaction. By increasing the CH_4 conversion under light, the product selectivity may then shift significantly by limiting the influence of RWGS. While promoting CH_4 conversion with light illumination may be advantageous to the activity and stability, it may be detrimental to the activity, as light-facilitated CH_4 dehydrogenation may inadvertently lead to complete CH_4 cracking, resulting in carbon accumulation.

The impact of visible light on the DRM reaction mechanism remains contentious. Several authors showed using isotopic DRIFTS that the LSPR promotes the formation of the methoxy (CH_xO_{ads}) intermediate by stimulating the release of O_{ads} trapped in the oxygen vacancies of a CeO_2-based support. Oxidation of the CH_x intermediate prevents complete CH_4 dehydrogenation (CH_4 cracking reaction), suppressing coke formation. Other authors attributed the improved stability to enhanced gasification of adsorbed carbon by releasing O_{ads}. Regardless of the pathway, studies suggest that O_{ads} release could be attributed to the oxygen storage capacity and facile reduction of CeO_2, which warrants further investigation.

Conversely, several studies have demonstrated catalyst deactivation by carbon deposition under visible light illumination, even in the presence of supports with oxygen release capacity (including CeO_2). Literature agrees that in addition to the light-promoted release of O_{ads}, light facilitates the adsorption and disassociation of CH_x on the active metal. The dual functionality of light unveils a delicate interplay between the light-accelerated CH_x dehydrogenation (that may inadvertently cause CH_4 cracking to C_{ads}) and the CH_x oxidation rate that either removes C_{ads} or avoids coke formation by forming CH_xO (x = 1–3). Future work should focus on probing this balance and understanding how material selection and modification of physicochemical properties influence the relative CH_x dehydrogenation and oxidation rates. Studies that have inadvertently probed this balance suggest that oxygen availability is crucial to improving stability under light.

Light-assisted thermocatalytic DRM is an emerging field with several key research barriers. Most significantly, there is a lack of understanding of the influence of material properties on the light-assisted DRM performance and the reaction mechanism. Although several supports have been studied, no systematic study has effectively investigated the oxygen release capacity of the support and associated physicochemical properties, such as the oxygen storage capacity, oxygen mobility, surface basicity and metal-support interaction in the context of light-assisted DRM. Similarly, the role of the active metal and influence of active metal properties (loading, dispersion and deposit size) has not been related to the light-assisted reaction mechanism or catalytic performance metrics such as selectivity and stability. Furthermore, decoupling the synergistic influence of light and thermal activity and understanding the role and relative contributions of hot electrons and localised hotspotting remains another significant research barrier for light-assisted DRM and beyond for LSPR-mediated catalysis. Understanding the physics behind the influence of light on the DRM mechanism may considerably aid the optimisation of the catalyst and process conditions. To address these research challenges, we propose several recommendations to advance the field:

(1) A systematic investigation into the role of the oxygen release capacity of the support in the light-assisted DRM mechanism. Systematically improving the oxygen release capacity may accomplish a complete understanding of the role of the support in improving catalytic stability.
(2) A systematic investigation into the role of the active metal on the light-assisted DRM mechanism. Carefully moderating the active metal properties such as loading, dispersion and active metal size may provide a more detailed understanding of how light influences the reaction mechanism and aid further catalyst optimisation.
(3) A catalyst universality study. Currently, a wide range of material combinations have been investigated for light-assisted DRM, but changes in the experimental conditions, such as reaction temperature, GHSV, CO_2/CH_4 ratio and light illumination conditions, limit direct comparability. Universality studies that investigate various supports and active metals will provide a more thorough basis for material selection and catalyst optimisation.
(4) A systematic investigation into the coupling of bandgap excitation and LSPR effects. Many photothermal studies have illuminated the catalysts with a broad solar spectrum, potentially resulting in both bandgap excitation and LSPR effects [9]. However, no study to date has decoupled these effects, limiting the understanding of the mechanism for the influence of light.
(5) A detailed techno-economic analysis on light-assisted DRM. Much of the recent work in light-assisted DRM has not been translated to the broader motivation of utilising CO_2 to mitigate the impacts of global warming. Performing this analysis and comparing it with technologies such as thermocatalytic DRM and other CO_2 reforming reactions like CO_2 methanation may provide a more thorough understanding of the requirements to become technologically competitive.
(6) Explore the use of artificial intelligence (AI) and machine learning in the design and optimisation of light-assisted DRM catalysts. Integrating LSPR into thermocatalyst design is an additional complexity that requires the careful balancing of (i) maximising the role of light (the light absorption properties of the catalyst, energy redistribution efficiency, wavelength and intensity of the light source), (ii) properties of the active metal (selection, loading and metal size) and (iii) properties of the support (oxygen release capacity, morphology, surface area, thermal stability), (iv) the various reaction parameters (outlined in (3) above) and (v) the synergistic effects of (i), (ii), (iii) and (iv). Using empirical and theoretical data, machine learning may be able to predict the catalytic performance of certain catalysts under light, as demonstrated by Haghshenas et al. [148], or AI-driven High-Throughput Experimentation (HTE) may provide the permutations necessary to rapidly optimise the catalyst, yielding catalyst suggestions tailored to the desired output [149].

These studies will provide a comprehensive understanding of the materials and their influence on light-assisted DRM mechanism, leading to ideal catalyst pairings and material property optimisation. Through efficient catalyst design, light can be employed as a tool to overcome common DRM limitations such as high thermal requirement, poor DRM promotion amongst possible side reactions, susceptibility to catalyst deactivation and active metal sintering.

Author Contributions

G.E.P.O., E.C.L., J.S. and R.A. conceptualised the project. G.E.P.O. wrote the manuscript, and E.C.L. and J.S. edited and commented on the manuscript. All authors who contributed to this work discussed the results and declared no conflict of interest.

Ethics Statement

Not applicable.

Informed Consent Statement

Not applicable.

Data Availability Statement

Not applicable.

Funding

This work was supported by the Australian Research Council (ARC) (DE230100789, DP230101864 and IC200100023).

Declaration of Competing Interest

The authors declare that they have no known competing financial interests or personal relationships that could have appeared to influence the work reported in this paper.

References

1. IPCC. *Climate Change 2023: Synthesis Report. Contribution of Working Groups I, II and III to the Sixth Assessment Report of the Intergovernmental Panel on Climate Change*; IPCC: Geneva, Switzerland, 2023. doi:10.59327/IPCC/AR6-9789291691647.
2. UNFCCC. Paris Agreement. In *Report, Proceedings of the 21st Session Parties to the United Nations Framework Convention on Climate Change, Paris, France, 12 December 2015*; United Nations Framework Convention on Climate Change: Bonn, Germany, 2015; p. 2017.
3. IPCC. *Summary for Policymakers of Global Warming of 1.5 °C: An IPCC Special Report*; Intergovernmental Panel on Climate Change: Geneva, Switzerland, 2018; pp. 3–24.
4. Turakulov Z, Kamolov A, Norkobilov A, Variny M, Díaz-Sainz G, Gómez-Coma L, et al. Assessing various CO_2 utilization technologies: a brief comparative review. *J. Chem. Technol. Biotechnol.* **2024**, *99*, 1291–1307. doi:10.1002/jctb.7606.
5. Aramouni NAK, Touma JG, Tarboush BA, Zeaiter J, Ahmad MN. Catalyst design for dry reforming of methane: Analysis review. *Renew. Sustain. Energy Rev.* **2018**, *82*, 2570–2585. doi:10.1016/j.rser.2017.09.076.
6. Bridgwater AV. Renewable fuels and chemicals by thermal processing of biomass. *Chem. Eng. J.* **2003**, *91*, 87–102. doi:10.1016/S1385-8947(02)00142-0.
7. Alhassan AM, Hussain I, Taialla OA, Awad MM, Tanimu A, Alhooshani K, et al. Advances in catalytic dry reforming of methane (DRM): Emerging trends, current challenges, and future perspectives. *J. Clean. Prod.* **2023**, *423*, 138638. doi:10.1016/j.jclepro.2023.138638.
8. Awad MM, Kotob E, Taialla OA, Hussain I, Ganiyu SA, Alhooshani K. Recent developments and current trends on catalytic dry reforming of methane: Hydrogen production, thermodynamics analysis, techno feasibility, and machine learning. *Energy Convers. Manag.* **2024**, *304*, 118252. doi:10.1016/j.enconman.2024.118252.
9. Tian X, Wang F. A review on catalyst advances for photothermal dry reforming of methane reaction. *Sep. Purif. Technol.* **2025**, *354*, 128799. doi:10.1016/j.seppur.2024.128799.
10. Ji G, Wu S, Song X, Meng L, Jia Y, Tian J. Recent progress in photo-thermal synergistic catalysis for methane dry reforming. *Int. J. Hydrogen Energy* **2024**, *57*, 696–708. doi:10.1016/j.ijhydene.2024.01.105.
11. Yin S-Y, Li Z, Hu Y, Luo X, Li J. A novel metal-free porous covalent organic polymer for efficient room-temperature photocatalytic CO_2 reduction via dry-reforming of methane. *Green Energy Environ.* **2024**, *9*, 1407–1418. doi:10.1016/j.gee.2023.03.003.
12. Huang Y, Xiong J, Li Z, Mao Y, Huang Y, Liang Z, et al. Insights into the role of S-Ti-O bond in titanium-based catalyst for photocatalytic CH4 reforming: Experimental and DFT exploration. *Chem. Eng. Sci.* **2024**, *289*, 119879. doi:10.1016/j.ces.2024.119879.
13. He C, Li Q, Ye Z, Wang L, Gong Y, Li S, et al. Regulating atomically-precise Pt sites for boosting light-driven dry reforming of methane. *Angew. Chem. Int. Ed.* **2024**, *63*, e202412308. doi:10.1002/anie.202412308.
14. Cho Y, Shoji S, Yamaguchi A, Hoshina T, Fujita T, Abe H, et al. Visible-light-driven dry reforming of methane using a semiconductor-supported catalyst. *Chem. Commun.* **2020**, *56*, 4611–4614. doi:10.1039/D0CC00729C.
15. Lavoie J-M. Review on dry reforming of methane, a potentially more environmentally-friendly approach to the increasing natural gas exploitation. *Front. Chem.* **2014**, *2*, 81. doi:10.3389/fchem.2014.00081.
16. Abdulrasheed A, Jalil AA, Gambo Y, Ibrahim M, Hambali HU, Hamid MS. A review on catalyst development for dry reforming of methane to syngas: Recent advances. *Renew. Sustain. Energy Rev.* **2019**, *108*, 175–193. doi:10.1016/j.rser.2019.03.054.
17. Hussien AGS, Polychronopoulou K. A review on the different aspects and challenges of the dry reforming of methane (DRM) reaction. *Nanomaterials* **2022**, *12*, 3400. doi:10.3390/nano12193400.
18. Ding M, Yang Y, Li Y, Wang T, Ma L, Wu C. Impact of H_2/CO ratios on phase and performance of Mn-modified Fe-based Fischer-Tropsch synthesis catalyst. *Appl. Energy* **2013**, *112*, 1241–1246. doi:10.1016/j.apenergy.2012.12.052.
19. Sun L, Wang Y, Guan N, Li L. Methane Activation and Utilization: Current Status and Future Challenges. *Energy Technol.* **2020**, *8*, 1900826. doi:10.1002/ente.201900826.
20. Wang C, Su Y, Tavasoli A, Sun W, Wang L, Ozin GA, et al. Recent advances in nanostructured catalysts for photo-assisted dry reforming of methane. *Mater. Today Nano* **2021**, *14*, 100113. doi:10.1016/j.mtnano.2021.100113.
21. Usman M, Daud WMAW, Abbas HF. Dry reforming of methane: Influence of process parameters—A review. *Renew. Sustain. Energy Rev.* **2015**, *45*, 710–744. doi:10.1016/j.rser.2015.02.026.
22. Al-Fatesh AS, Patel N, Fakeeha AH, Alotibi MF, Alreshaidan SB, Kumar R. Reforming of methane: Effects of active metals, supports, and promoters. *Catal. Rev.* **2023**, *10,* 1734. doi:10.1080/01614940.2023.2211447.

23. Lovell E. *Closing the Carbon Loop: Activating Nickel Catalysts for the Carbon Dioxide Reforming of Methane*; University of Bath: Bath, UK, 2016.
24. Papadopoulou C, Matralis H, Verykios X. Utilization of biogas as a renewable carbon source: Dry reforming of methane. In *Catalysis for Alternative Energy Generation*; Springer: New York, NY, USA, 2012; pp. 57–127. doi:10.1007/978-1-4614-0344-9_3.
25. Liu H, Dao TD, Liu L, Meng X, Nagao T, Ye J. Light assisted CO_2 reduction with methane over group VIII metals: Universality of metal localized surface plasmon resonance in reactant activation. *Appl. Catal. B* **2017**, *209*, 183–189. doi:10.1016/j.apcatb.2017.02.080.
26. Liu H, Meng X, Dao TD, Zhang H, Li P, Chang K, et al. Conversion of carbon dioxide by methane reforming under visible-light irradiation: Surface-plasmon-mediated nonpolar molecule activation. *Angew. Chem.* **2015**, *127*, 11707–11711. doi:10.1002/anie.201504933.
27. Song H, Meng X, Dao TD, Zhou W, Liu H, Shi L, et al. Light-enhanced carbon dioxide activation and conversion by effective plasmonic coupling effect of Pt and Au nanoparticles. *ACS Appl. Mater. Interfaces* **2018**, *10*, 408–416. doi:10.1021/acsami.7b13043.
28. Zhou L, Martirez JMP, Finzel J, Zhang C, Swearer DF, Tian S, et al. Light-driven methane dry reforming with single atomic site antenna-reactor plasmonic photocatalysts. *Nat. Energy* **2020**, *5*, 61–70. doi:10.1038/s41560-019-0517-9.
29. Torrez-Herrera JJ, Korili SA, Gil A. Recent progress in the application of Ni-based catalysts for the dry reforming of methane. *Catal. Rev.* **2023**, *65*, 1300–1357. doi:10.1080/01614940.2021.2006891.
30. Wang Y, Yao L, Wang Y, Wang S, Zhao Q, Mao D, et al. Low-temperature catalytic CO_2 dry reforming of methane on Ni-Si/ZrO_2 catalyst. *ACS Catal.* **2018**, *8*, 6495–6506. doi:10.1021/acscatal.8b00584.
31. Lorber K, Zavašnik J, Sancho-Parramon J, Bubaš M, Mazaj M, Djinović P. On the mechanism of visible-light accelerated methane dry reforming reaction over Ni/CeO_{2-x} catalysts. *Appl. Catal. B* **2022**, *301*, 120745. doi:10.1016/j.apcatb.2021.120745.
32. Li Y, Wang Y, Zhang X, Mi Z. Thermodynamic analysis of autothermal steam and CO_2 reforming of methane. *Int. J. Hydrogen Energy* **2008**, *33*, 2507–2514. doi:10.1016/j.ijhydene.2008.02.051.
33. Nikoo MK, Amin NAS. Thermodynamic analysis of carbon dioxide reforming of methane in view of solid carbon formation. *Fuel Process. Technol.* **2011**, *92*, 678–691. doi:10.1016/j.fuproc.2010.11.027.
34. Abdulrasheed AA, Jalil AA, Siang TJ, Hambali HU. Thermodynamic sensitivity analysis of CO_2 reforming of methane based on equilibrium predictions. In *IOP Conference Series: Materials Science and Engineering*; IOP Publishing: Bristol, UK, 2020; Volume 808, p. 012001. doi:10.1088/1757-899X/808/1/012001.
35. Rostrup-Nielsen JR, Hansen JHB. CO_2-reforming of methane over transition metals. *J. Catal.* **1993**, *144*, 38–49. doi:10.1006/jcat.1993.1312.
36. Li J, Li J, Zhu Q. Carbon deposition and catalytic deactivation during CO_2 reforming of CH4 over Co/MgO catalyst. *Chin. J. Chem. Eng.* **2018**, *26*, 2344–2350. doi:10.1016/j.cjche.2018.05.025.
37. Bitters JS, He T, Nestler E, Senanayake SD, Chen JG, Zhang C, et al. Utilizing bimetallic catalysts to mitigate coke formation in dry reforming of methane. *J. Energy Chem.* **2022**, *68*, 124–142. doi:10.1016/j.jechem.2021.11.041.
38. Arora S, Prasad R. An overview on dry reforming of methane: Strategies to reduce carbonaceous deactivation of catalysts. *RSC Adv.* **2016**, *6*, 108668–108688. doi:10.1039/C6RA20450C.
39. Rostrup-Nielsen JR. *Catalysis, Science and Technology*; Springer: Berlin, Germany, 1984.
40. Ruckenstein E, Wang HY. Carbon deposition and catalytic deactivation during CO_2 reforming of CH_4 over Co/γ-Al_2O_3 catalysts. *J. Catal.* **2002**, *205*, 289–293. doi:10.1006/jcat.2001.3458.
41. Ghaib K, Nitz K, Ben-Fares F. Chemical methanation of CO_2: A review. *ChemBioEng Rev.* **2016**, *3*, 266–275. doi:10.1002/cite.201600066.
42. Nagaoka K, Okamura M, Aika K. Titania supported ruthenium as a coking-resistant catalyst for high pressure dry reforming of methane. *Catal. Commun.* **2001**, *2*, 255–260. doi:10.1016/S1566-7367(01)00043-7.
43. He Z, Gong K, Wei Y, Dai Y, Zhu L, Gao K, et al. Engineering an Ni-TiO_x interface for highly active and durable solar-driven dry reforming of methane. *Chem Catal.* **2024**, *4*, 101040. doi:10.1016/j.checat.2024.101040.
44. Rönsch S, Schneider J, Matthischke S, Schlüter M, Götz M, Lefebvre J, et al. Review on methanation—From fundamentals to current projects. *Fuel* **2016**, *166*, 276–296. doi:10.1016/j.fuel.2015.10.111.
45. Wang D, Chen Y, Fan L, Xiao T, Meng T, Xing Z, et al. Bulk and surface dual modification of nickel-cobalt spinel with ruthenium toward highly efficient overall water splitting. *Appl. Catal. B* **2022**, *305*, 121081. doi:10.1016/j.apcatb.2022.121081.
46. Hou Z, Chen P, Fang H, Zheng X, Yashima T. Production of synthesis gas via methane reforming with CO_2 on noble metals and small amount of noble-(Rh-) promoted Ni catalysts. *Int. J. Hydrogen Energy* **2006**, *31*, 555–561. doi:10.1016/j.ijhydene.2005.06.010.
47. Li L, Zeng W, Song M, Wu X, Li G, Hu C. Research Progress and Reaction Mechanism of CO_2 Methanation over Ni-Based Catalysts at Low Temperature: A Review. *Catalysts* **2022**, *12*, 244. doi:10.3390/catal12020244.

48. Guo S, Sun Y, Zhang Y, Zhang C, Li Y, Bai J. Bimetallic Nickel-Cobalt catalysts and their application in dry reforming reaction of methane. *Fuel* **2024**, *358*, 130290. doi:10.1016/j.fuel.2023.130290.
49. Rego de Vasconcelos B, Pham Minh D, Lyczko N, Phan TS, Sharrock P, Nzihou A. Upgrading greenhouse gases (methane and carbon dioxide) into syngas using nickel-based catalysts. *Fuel* **2018**, *226*, 195–203. doi:10.1016/j.fuel.2018.04.017.
50. Alarcón A, Guilera J, Soto R, Andreu T. Higher tolerance to sulfur poisoning in CO_2 methanation by the presence of CeO_2. *Appl. Catal. B* **2020**, *263*, 118346. doi:10.1016/j.apcatb.2019.118346.
51. Zhan Y, Song K, Shi Z, Wan C, Pan J, Li D, et al. Influence of reduction temperature on Ni particle size and catalytic performance of Ni/Mg(Al)O catalyst for CO_2 reforming of CH_4. *Int. J. Hydrogen Energy* **2020**, *45*, 2794–2807. doi:10.1016/j.ijhydene.2019.11.181.
52. Guharoy U, Reina TR, Liu J, Sun Q, Gu S, Cai Q. A theoretical overview on the prevention of coking in dry reforming of methane using non-precious transition metal catalysts. *J. CO2 Util.* **2021**, *53*, 101728. doi:10.1016/j.jcou.2021.101728.
53. Qin Z, Chen J, Xie X, Luo X, Su T, Ji H. CO_2 reforming of CH_4 to syngas over nickel-based catalysts. *Environ. Chem. Lett.* **2020**, *18*, 997–1017. doi:10.1007/s10311-020-00996-w.
54. Takanabe K, Nagaoka K, Nariai K, Aika K. Titania-supported cobalt and nickel bimetallic catalysts for carbon dioxide reforming of methane. *J. Catal.* **2005**, *232*, 268–275. doi:10.1016/j.jcat.2005.03.011.
55. Zhang J, Xie K, Jiang Y, Li M, Tan X, Yang Y, et al. Photoinducing different mechanisms on a Co-Ni bimetallic alloy in catalytic dry reforming of methane. *ACS Catal.* **2023**, *13*, 10855–10865. doi:10.1021/acscatal.3c02525.
56. Horlyck J, Lawrey C, Lovell EC, Amal R, Scott J. Elucidating the impact of Ni and Co loading on the selectivity of bimetallic NiCo catalysts for dry reforming of methane. *Chem. Eng. J.* **2018**, *352*, 572–580. doi:10.1016/j.cej.2018.07.009.
57. Luisetto I, Tuti S, Di Bartolomeo E. Co and Ni supported on CeO_2 as selective bimetallic catalyst for dry reforming of methane. *Int. J. Hydrogen Energy* **2012**, *37*, 15992–15999. doi:10.1016/j.ijhydene.2012.08.006.
58. Chen S, Zaffran J, Yang B. Dry reforming of methane over the cobalt catalyst: Theoretical insights into the reaction kinetics and mechanism for catalyst deactivation. *Appl. Catal. B* **2020**, *270*, 118859. doi:10.1016/j.apcatb.2020.118859.
59. Khairudin NF, Mohammadi M, Mohamed AR. An investigation on the relationship between physicochemical characteristics of alumina-supported cobalt catalyst and its performance in dry reforming of methane. *Environ. Sci. Pollut. Res.* **2021**, *28*, 29157–29176. doi:10.1007/s11356-021-12794-0.
60. Wang HY, Ruckenstein E. CO_2 reforming of CH_4 over Co/MgO solid solution catalysts—effect of calcination temperature and Co loading. *Appl. Catal. A Gen.* **2001**, *209*, 207–215. doi:10.1016/S0926-860X(00)00753-5.
61. Djinović P, Osojnik Črnivec IG, Erjavec B, Pintar A. Influence of active metal loading and oxygen mobility on coke-free dry reforming of Ni–Co bimetallic catalysts. *Appl. Catal. B* **2012**, *125*, 259–270. doi:10.1016/j.apcatb.2012.05.049.
62. Ewbank JL, Kovarik L, Diallo FZ, Sievers C. Effect of metal–support interactions in Ni/Al_2O_3 catalysts with low metal loading for methane dry reforming. *Appl. Catal. A Gen.* **2015**, *494*, 57–67. doi:10.1016/j.apcata.2015.01.029.
63. Damaskinos CM, Zavašnik J, Djinović P, Efstathiou AM. Dry reforming of methane over $Ni/Ce_{0.8}Ti_{0.2}O_{2-\delta}$: The effect of Ni particle size on the carbon pathways studied by transient and isotopic techniques. *Appl. Catal. B* **2021**, *296*, 120321. doi:10.1016/j.apcatb.2021.120321.
64. Chen J, Zhang Y, Zhang Z, Hou D, Bai F, Han Y, et al. Metal–support interactions for heterogeneous catalysis: mechanisms, characterization techniques and applications. *J. Mater. Chem. A* **2023**, *11*, 8540–8572. doi:10.1039/D2TA10036C.
65. Wang HY, Ruckenstein E. Carbon dioxide reforming of methane to synthesis gas over supported rhodium catalysts: the effect of support. *Appl. Catal. A Gen.* **2000**, *204*, 143–152. doi:10.1016/S0926-860X(00)00547-0.
66. Zhang R, Xi Z, Li M, Yu W, Nie H, Li D. Effect of support on the performance of Ni-based catalyst in methane dry reforming. *J. Fuel Chem. Technol.* **2015**, *43*, 1359–1365. doi:10.1016/S1872-5813(15)30040-2.
67. Awad MM, Hussain I, Mustapha U, Taialla OA, Alhassan AM, Kotob E, et al. A critical review of recent advancements in catalytic dry reforming of methane: Physicochemical properties, current challenges, and informetric insights. *Int. J. Hydrogen Energy* **2024**, *76*, 202–233. doi:10.1016/j.ijhydene.2024.03.319.
68. Aw MS, Dražić G, Djinović P, Pintar A. Transition metal pairs on ceria-promoted, ordered mesoporous alumina as catalysts for the CO_2 reforming reaction of methane. *Catal. Sci. Technol.* **2016**, *6*, 3797–3805. doi:10.1039/C5CY02082D.
69. Littlewood P, Liu S, Weitz E, Marks TJ, Stair PC. Ni-alumina dry reforming catalysts: Atomic layer deposition and the issue of Ni aluminate. *Catal. Today* **2020**, *343*, 18–25. doi:10.1016/j.cattod.2019.03.040.
70. Zhou L, Li L, Wei N, Li J, Basset J-M. Effect of $NiAl_2O_4$ Formation on Ni/Al_2O_3 Stability during Dry Reforming of Methane. *ChemCatChem* **2015**, *7*, 2508–2516. doi:10.1002/cctc.201500379.
71. Horlyck J, Pokhrel S, Lovell E, Bedford NM, Mädler L, Amal R, et al. Unifying double flame spray pyrolysis with lanthanum doping to restrict cobalt–aluminate formation in Co/Al_2O_3 catalysts for the dry reforming of methane. *Catal. Sci. Technol.* **2019**, *9*, 4970–4980. doi:10.1039/c9cy01293a.
72. Liu Z, Li J, Buettner M, Ranganathan RV, Uddi M, Wang R. Metal–Support Interactions in CeO_2- and SiO_2-Supported Cobalt Catalysts: Effect of Support Morphology, Reducibility, and Interfacial Configuration. *ACS Appl. Mater. Interfaces* **2019**, *11*, 17035–17049. doi:10.1021/acsami.9b02455.
73. Selvarajan V, Obuobi S, Ee PLR. Silica Nanoparticles—A Versatile Tool for the Treatment of Bacterial Infections. *Front.*

*Chem.***2020**, *8*, 00602. doi:10.3389/fchem.2020.00602.
74. Ekeoma BC, Yusuf M, Johari K, Abdullah B. Mesoporous silica supported Ni-based catalysts for methane dry reforming: A review of recent studies. *Int. J. Hydrogen Energy* **2022**, *47*, 41596–41620. doi:10.1016/j.ijhydene.2022.05.297.
75. Liu H, Meng X, Dao TD, Liu L, Li P, Zhao G, et al. Light assisted CO_2 reduction with methane over SiO_2 encapsulated Ni nanocatalysts for boosted activity and stability. *J. Mater. Chem.* A **2017**, *5*, 10567–10573. doi:10.1039/C7TA00704C.
76. Zhang Y, Zhang G, Liu J, Li T, Wang Y, Zhao Y, et al. Dry reforming of methane over Ni/SiO_2 catalysts: Role of support structure properties. *Fuel* **2023**, *340*, 127490. doi:10.1016/j.fuel.2023.127490.
77. Nagaoka K, Takanabe K, Aika K. Influence of the phase composition of titania on catalytic behavior of Co/TiO_2 for the dry reforming of methane. *Chem. Commun.* **2002**, *9*, 1006–1007. doi:10.1039/B201717M.
78. Shah M, Al Mesfer MK, Danish M. Effect of titania synthesis conditions on the catalytic performance of mesoporous Ni/TiO_2 catalysts for carbon dioxide reforming of methane. *Int. J. Hydrogen Energy* **2022**, *47*, 8867–8874. doi:10.1016/j.ijhydene.2021.12.246.
79. Teh LP, Setiabudi HD, Timmiati SN, Aziz MAA, Annuar NHR, Ruslan NN. Recent progress in ceria-based catalysts for the dry reforming of methane: A review. *Chem. Eng. Sci.* **2021**, *242*, 116606. doi:10.1016/j.ces.2021.116606.
80. Manan WN, Wan Isahak WN, Yaakob Z. CeO_2-Based Heterogeneous Catalysts in Dry Reforming Methane and Steam Reforming Methane: A Short Review. *Catalysts* **2022**, *12*, 452. doi:10.3390/catal12050452.
81. Cárdenas-Arenas A, Quindimil A, Davó-Quiñonero A, Bailón-García E, Lozano-Castello D, De-La-Torre U, et al. Isotopic and in situ DRIFTS study of the CO_2 methanation mechanism using Ni/CeO_2 and Ni/Al_2O_3 catalysts. *Appl. Catal. B* **2020**, *265*, 118538. doi:10.1016/j.apcatb.2019.118538.
82. Xiao M, Zhang X, Yang Y, Cui X, Chen T, Wang Y. M (M= Mn, Co, Cu)-CeO_2 catalysts to enhance their CO catalytic oxidation at a low temperature: Synergistic effects of the interaction between Ce^{3+}-Mx^{+}-Ce^{4+} and the oxygen vacancy defects. *Fuel* **2022**, *323*, 124379. doi:10.1016/j.fuel.2022.124379.
83. Damaskinos CM, Vasiliades MA, Efstathiou AM. The effect of Ti^{4+} dopant in the 5 wt% Ni/$Ce_{1-x}Ti_xO_{2-\delta}$ catalyst on the carbon pathways of dry reforming of methane studied by various transient and isotopic techniques. *Appl. Catal. A Gen.* **2019**, *579*, 116–129. doi:10.1016/j.apcata.2019.04.023.
84. Vasiliades MA, Djinović P, Davlyatova LF, Pintar A, Efstathiou AM. Origin and reactivity of active and inactive carbon formed during DRM over Ni/$Ce_{0.38}Zr_{0.62}O_{2-\delta}$ studied by transient isotopic techniques. *Catal. Today* **2018**, *299*, 201–211. doi:10.1016/j.cattod.2017.03.057.
85. Rao Z, Wang K, Cao Y, Feng Y, Huang Z, Chen Y, et al. Light-Reinforced Key Intermediate for Anticoking To Boost Highly Durable Methane Dry Reforming over Single Atom Ni Active Sites on CeO_2. *J. Am. Chem. Soc.* **2023**, *145*, 24625–24635. doi:10.1021/jacs.3c07077.
86. Osazuwa OU, Abidin SZ, Fan X, Amenaghawon AN, Azizan MT. An Insight into the Effects of Synthesis Methods on Catalysts Properties for Methane Reforming. *J. Environ. Chem. Eng.* **2021**, *9*, 105052. doi:10.1016/j.jece.2021.105052.
87. Baharudin L, Rahmat N, Othman NH, Shah N, Syed-Hassan SSA. Formation, Control, and Elimination of Carbon on Ni-Based Catalyst during CO_2 and CH_4 Conversion via Dry Reforming Process: A Review. *J. CO_2 Util.* **2022**, *61*, 102050. doi:10.1016/j.jcou.2022.102050.
88. Wang S, Lu GQ, Millar GJ. Carbon Dioxide Reforming of Methane To Produce Synthesis Gas over Metal-Supported Catalysts: State of the Art. *Energy Fuels* **1996**, *10*, 896–904. doi:10.1021/ef950227t.
89. Alvarez Moreno A, Ramirez-Reina T, Ivanova S, Roger A-C, Centeno MÁ, Odriozola JA. Bimetallic Ni–Ru and Ni–Re Catalysts for Dry Reforming of Methane: Understanding the Synergies of the Selected Promoters. *Front. Chem.* **2021**, *9*. doi:10.3389/fchem.2021.694976.
90. Li D, Nakagawa Y, Tomishige K. Methane Reforming to Synthesis Gas over Ni Catalysts Modified with Noble Metals. *Appl. Catal. A Gen.* **2011**, *408*, 1–24. doi:10.1016/j.apcata.2011.09.018.
91. Franz R, Kühlewind T, Shterk G, Abou-Hamad E, Parastaev A, Uslamin E, et al. Impact of Small Promoter Amounts on Coke Structure in Dry Reforming of Methane over Ni/ZrO_2. *Catal. Sci. Technol.* **2020**, *10*, 3965–3974. doi:10.1039/D0CY00817F.
92. Cazorla-Amorós D, Linares-Solano A, Dekker FHM, Kapteijn F. Isotopic Steady-State and Step-Response Study on Carbon Gasification Catalyzed by Calcium. *Carbon* **1995**, *33*, 1147–1154. doi:10.1016/0008-6223(95)00068-O.
93. Chen SG, Yang RT. Unified Mechanism of Alkali and Alkaline Earth Catalyzed Gasification Reactions of Carbon by CO_2 and H_2O. *Energy Fuels* **1997**, *11*, 421–427. doi:10.1021/ef960099o.
94. Ibrahim AA, Al-Fatesh AA, Atia H, Fakeeha AH, Kasim SO, Abasaeed AE. Influence of Promoted 5%Ni/MCM-41 Catalysts on Hydrogen Yield in CO_2 Reforming of CH_4. *Int. J. Energy Res.* **2018**, *42*, 4120–4130. doi:10.1002/er.4156.
95. Byron C, Ferrandon MS, Kropf AJ, Delferro M, Teplyakov AV. Surface Basic Site Effect on Boron-Promoted Platinum Catalysts for Dry Reforming of Methane. *J. Phys. Chem. C* **2023**, *127*, 24137–24148. doi:10.1021/acs.jpcc.3c05724.
96. Fouskas A, Kollia M, Kambolis A, Papadopoulou C, Matralis H. Boron-Modified Ni/Al_2O_3 Catalysts for Reduced Carbon Deposition during Dry Reforming of Methane. *Appl. Catal. A Gen.* **2014**, *474*, 125–134. doi:10.1016/j.apcata.2013.08.016.
97. Al Abdulghani AJ, Park J-H, Kozlov SM, Kang D-C, AlSabban B, Pedireddy S, et al. Methane Dry Reforming on Supported

Cobalt Nanoparticles Promoted by Boron. *J. Catal.* **2020**, *392*, 126–134. doi:10.1016/j.jcat.2020.09.015.
98. Horváth A, Németh M, Beck A, Maróti B, Sáfrán G, Pantaleo G, et al. Strong Impact of Indium Promoter on Ni/Al2O3 and Ni/CeO_2-Al_2O_3 Catalysts Used in Dry Reforming of Methane. *Appl. Catal. A Gen.* **2021**, *621*, 118174. doi:10.1016/j.apcata.2021.118174.
99. Laosiripojana N, Sutthisripok W, Assabumrungrat S. Synthesis Gas Production from Dry Reforming of Methane over CeO_2 Doped Ni/Al_2O_3: Influence of the Doping Ceria on the Resistance toward Carbon Formation. *Chem. Eng. J.* **2005**, *112*, 13–22. doi:10.1016/j.cej.2005.06.003.
100. Alipour Z, Rezaei M, Meshkani F. Effect of Alkaline Earth Promoters (MgO, CaO, and BaO) on the Activity and Coke Formation of Ni Catalysts Supported on Nanocrystalline Al_2O_3 in Dry Reforming of Methane. *J. Ind. Eng. Chem.* **2014**, *20*, 2858–2863. doi:10.1016/j.jiec.2013.11.018.
101. Chaudhary PK, Koshta N, Deo G. Effect of O_2 and temperature on the catalytic performance of Ni/Al_2O_3 and Ni/$MgAl_2O_4$ for the dry reforming of methane (DRM). *Int. J. Hydrogen Energy* **2020**, *45*, 4490–4500. doi:10.1016/j.ijhydene.2019.12.053.
102. Kambolis A, Matralis H, Trovarelli A, Papadopoulou C. Ni/CeO_2-ZrO_2 catalysts for the dry reforming of methane. *Appl. Catal. A Gen.* **2010**, *377*, 16–26. doi:10.1016/j.apcata.2010.01.013.
103. Montoya JA, Romero-Pascual E, Gimon C, Del Angel P, Monzón A. Methane reforming with CO_2 over Ni/ZrO_2–CeO_2 catalysts prepared by sol–gel. *Catal. Today* **2000**, *63*, 71–85. doi:10.1016/S0920-5861(00)00447-8.
104. Vasiliades MA, Makri MM, Djinović P, Erjavec B, Pintar A, Efstathiou AM. Dry reforming of methane over 5 wt% Ni/Ce1-xPrx$O_{2-\delta}$ catalysts: Performance and characterisation of active and inactive carbon by transient isotopic techniques. *Appl. Catal. B* **2016**, *197*, 168–183. doi:10.1016/j.apcatb.2016.03.012.
105. Xie B, Lovell E, Tan TH, Jantarang S, Yu M, Scott J, et al. Emerging material engineering strategies for amplifying photothermal heterogeneous CO_2 catalysis. *J. Energy Chem.* **2021**, *59*, 108–125. doi:10.1016/j.jechem.2020.11.005.
106. Ghoussoub M, Xia M, Duchesne PN, Segal D, Ozin G. Principles of photothermal gas-phase heterogeneous CO_2 catalysis. *Energy Environ. Sci.* **2019**, *12*, 1122–1142. doi:10.1039/C8EE02790K.
107. Rodrigues MS, Borges J, Lopes C, Pereira RMS, Vasilevskiy MI, Vaz F. Gas Sensors Based on Localized Surface Plasmon Resonances: Synthesis of Oxide Films with Embedded Metal Nanoparticles, Theory and Simulation, and Sensitivity Enhancement Strategies. *Appl. Sci.* **2021**, *11*, 5388. doi:10.3390/app11125388.
108. Yin T, Jiang L, Shen Z. Recent progress on photoluminescence from plasmonic nanostructures: Phenomenon, mechanism, and application. *Chin. Phys. B* **2018**, *27*, 097803. doi:10.1088/1674-1056/27/9/097803.
109. Fong KE, Yung L-YL. Localized surface plasmon resonance: A unique property of plasmonic nanoparticles for nucleic acid detection. *Nanoscale* **2013**, *5*, 12043–12071. doi:10.1039/C3NR02257A.
110. Petryayeva E, Krull UJ. Localized surface plasmon resonance: Nanostructures, bioassays and biosensing—A review. *Anal. Chim. Acta* **2011**, *706*, 8–24. doi:10.1016/j.aca.2011.08.020.
111. de Souza ML, dos Santos DP, Corio P. Localized surface plasmon resonance enhanced photocatalysis: An experimental and theoretical mechanistic investigation. *RSC Adv.* **2018**, *8*, 28753–28762. doi:10.1039/C8RA03919D.
112. Bora T. Recent Developments on Metal Nanoparticles for SERS Applications. In *Noble and Precious Metals-Properties, Nanoscale Effects and Applications*; InTechOpen: London, UK, 2018; pp.1–20.
113. Corma A, Garcia H. Photocatalytic reduction of CO_2 for fuel production: Possibilities and challenges. *J. Catal.* **2013**, *308*, 168–175. doi:10.1016/j.jcat.2013.06.008.
114. Chang X, Wang T, Gong J. CO_2 photo-reduction: insights into CO_2 activation and reaction on surfaces of photocatalysts. *Energy Environ. Sci.* **2016**, *9*, 2177–2196. doi:10.1039/C6EE00383D.
115. Zheng BY, Zhao H, Manjavacas A, McClain M, Nordlander P, Halas NJ. Distinguishing between plasmon-induced and photoexcited carriers in a device geometry. *Nat. Commun.* **2015**, *6*, 8797. doi:10.1038/ncomms8797.
116. Clavero C. Plasmon-induced hot-electron generation at nanoparticle/metal-oxide interfaces for photovoltaic and photocatalytic devices. *Nat. Photonics* **2014**, *8*, 95–101. doi:10.1038/nphoton.2013.238.
117. Inagaki T, Kagami K, Arakawa ET. Photoacoustic observation of nonradiative decay of surface plasmons in silver. *Phys. Rev. B* **1981**, *24*, 3644–3649. doi:10.1103/PhysRevB.24.3644.
118. Brongersma ML, Halas NJ, Nordlander P. Plasmon-induced hot carrier science and technology. *Nat. Nanotechnol.* **2015**, *10*, 25–34. doi:10.1038/nnano.2014.311.
119. Cortés E, Xie W, Cambiasso J, Jermyn AS, Sundararaman R, Narang P, et al. Plasmonic hot electron transport drives nano-localized chemistry. *Nat. Commun.* **2017**, *8*, 14880. doi:10.1038/ncomms14880.
120. Park JY, Kim SM, Lee H, Naik B. Hot electron and surface plasmon-driven catalytic reaction in metal–semiconductor nanostructures. *Catal. Lett.* **2014**, *144*, 1996–2004. doi:10.1007/s10562-014-1333-2.
121. Yu Y, Sundaresan V, Willets KA. Hot Carriers versus thermal effects: Resolving the enhancement mechanisms for plasmon-mediated photoelectrochemical reactions. *J. Phys. Chem. C* **2018**, *122*, 5040–5048. doi:10.1021/acs.jpcc.7b12080.
122. Gergen B, Nienhaus H, Weinberg WH, McFarland EW. Chemically induced electronic excitations at metal surfaces. *Science* **2001**, *294*, 2521–2523. doi:10.1126/science.1066134.

123. Ji X, Zuppero A, Gidwani JM, Somorjai GA. Electron flow generated by gas phase exothermic catalytic reactions using a platinum–gallium nitride nanodiode. *J. Am. Chem. Soc.* **2005**, *127*, 5792–5793. doi:10.1021/ja050945m.
124. Yu H, Peng Y, Yang Y, Li Z-Y. Plasmon-enhanced light–matter interactions and applications. *npj Comput. Mater.* **2019**, *5*, 45. doi:10.1038/s41524-019-0184-1.
125. Marimuthu A, Zhang J, Linic S. Tuning selectivity in propylene epoxidation by plasmon mediated photo-switching of Cu oxidation state. *Science* **2013**, *339*, 1590–1593. doi:10.1126/science.1231631.
126. Li R, Wang X, Chen M. Non-Noble Metal and Nonmetallic Plasmonic Nanomaterials with Located Surface Plasmon Resonance Effects: Photocatalytic Performance and Applications. *Catalysts* **2023**, *13*, 940. doi:10.3390/catal13060940.
127. Braik M, Sow I, Nelayah J, Belkhir A, Faustini M, Mercone S, et al. Introducing cobalt as a potential plasmonic candidate combining optical and magnetic functionalities within the same nanostructure. *Nanoscale* **2021**, *13*, 2639–2647. doi:10.1039/D0NR06966C.
128. Ullah S, Lovell EC, Tan TH, Xie B, Kumar PV, Amal R, et al. Photoenhanced CO_2 methanation over La_2O_3 promoted Co/TiO_2 catalysts. *Appl. Catal. B* **2021**, *294*, 120248. doi:10.1016/j.apcatb.2021.120248.
129. Zhou L, Swearer DF, Zhang C, Robatjazi H, Zhao H, Henderson L, et al. Quantifying hot carrier and thermal contributions in plasmonic photocatalysis. *Science* **2018**, *362*, 69–72. doi:10.1126/science.aat6967.
130. Zhang X, Li X, Reish ME, Zhang D, Su NQ, Gutiérrez Y, et al. Plasmon-enhanced catalysis: Distinguishing thermal and nonthermal effects. *Nano Lett.* **2018**, *18*, 1714–1723. doi:10.1021/acs.nanolett.7b04776.
131. Kim S, Kim J-M, Park J-E, Nam J-M. Nonnoble-metal-based plasmonic nanomaterials: Recent advances and future perspectives. *Adv. Mater.* **2018**, *30*, 1704528. doi:10.1002/adma.201704528.
132. Armaroli T, Bécue T, Gautier S. Diffuse Reflection Infrared Spectroscopy (DRIFTS): Application to the in situ analysis of catalysts. *Oil Gas Sci. Technol.* **2004**, *59*, 215–237. doi:10.2516/ogst:2004016.
133. Tan TH, Xie B, Ng YH, Abdullah SFB, Tang HYM, Bedford N, et al. Unlocking the potential of the formate pathway in the photo-assisted Sabatier reaction. *Nat. Catal.* **2020**, *3*, 1034–1043. doi:10.1038/s41929-020-00544-3.
134. O'Connell GEP, Webster RF, Elkington E, Amal R, Scott J, Lovell EC. Shining a light on methane dry reforming—exploring the impact of visible light on carbon formation over $Co/xCeO_2–Al_2O_3$. *Catal. Sci. Technol.* **2024**, *14*, 6790–6807. doi:10.1039/D4CY00925H.
135. Zhang Q, Mao M, Li Y, Yang Y, Huang H, Jiang Z, et al. Novel photoactivation promoted light-driven CO_2 reduction by CH_4 on Ni/CeO_2 nanocomposite with high light-to-fuel efficiency and enhanced stability. *Appl. Catal. B* **2018**, *239*, 555–564. doi:10.1016/j.apcatb.2018.08.052.
136. O'Connell GEP, Tan TH, Yuwono JA, Wang Y, Kheradmand A, Jiang Y, et al. Seeing the light: The role of cobalt in light-assisted CO_2 methanation. *Appl. Catal. B* **2024**, *343*, 123507. doi:10.1016/j.apcatb.2023.123507.
137. Zhu YF, Xie B, Yuwono JA, Kumar P, Sharma AS, Nielsen MP, et al. Making light work: Designing plasmonic structures for the selective photothermal methanation of carbon dioxide. *EES Catal.* **2024**, *2*, 834–849. doi:10.1039/D3EY00315A.
138. Tahir B, Tahir M, Amin NAS. Ag-La loaded protonated carbon nitrides nanotubes (pCNNT) with improved charge separation in a monolithic honeycomb photoreactor for enhanced bireforming of methane (BRM) to fuels. *Appl. Catal. B* **2019**, *248*, 167–183. doi:10.1016/j.apcatb.2019.01.076.
139. Liu H, Li M, Dao TD, Liu Y, Zhou W, Liu L, et al. Design of PdAu alloy plasmonic nanoparticles for improved catalytic performance in CO_2 reduction with visible light irradiation. *Nano Energy* **2016**, *26*, 398–404. doi:10.1016/j.nanoen.2016.05.045.
140. Liu H, Song H, Meng X, Yang L, Ye J. Light irradiation enhanced CO_2 reduction with methane: A case study in size-dependent optical property of Ni nanoparticles. *Catal. Today* **2019**, *335*, 187–192. doi:10.1016/j.cattod.2018.11.005.
141. Takami D, Yamamoto A, Yoshida H. Dry reforming of methane over alumina-supported rhodium catalysts at low temperatures under visible and near-infrared light. *Catal. Sci. Technol.* **2020**, *10*, 5811–5814. doi:10.1039/D0CY00858C.
142. Takami D, Ito Y, Kawaharasaki S, Yamamoto A, Yoshida H. Low temperature dry reforming of methane over plasmonic Ni photocatalysts under visible light irradiation. *Sustain. Energy Fuels* **2019**, *3*, 2968–2971. doi:10.1039/C9SE00206E.
143. Hu Q, Li Y, Cao H, Ji L, Wu J, Zhong M. Light-driven thermocatalytic CO_2 reduction by CH4 on alumina-cluster-modified Ni nanoparticles with excellent durability and high light-to-fuel efficiency promoted by the photoactivation effect. *J. Colloid Interface Sci.* **2024**, *657*, 942–952. doi:10.1016/j.jcis.2023.12.032.
144. Wu S, Li Y, Zhang Q, Jiang Z, Yang Y, Wu J, et al. High light-to-fuel efficiency and CO_2 reduction rates achieved on a unique nanocomposite of Co/Co doped Al_2O_3 nanosheets with UV-vis-IR irradiation. *Energy Environ. Sci.* **2019**, *12*, 2581–2590. doi:10.1039/C9EE01484E.
145. Liu X, Shi H, Meng X, Sun C, Zhang K, Gao L, et al. Solar-Enhanced CO_2 Conversion with CH_4 over Synergetic NiCo Alloy Catalysts with Light-to-Fuel Efficiency of 33.8%. *Solar RRL* **2021**, *5*, 2100185. doi:10.1002/solr.202100185.
146. Wu S, Li Y, Zhang Q, Hu Q, Wu J, Zhou C, et al. Formation of NiCo Alloy Nanoparticles on Co Doped Al_2O_3 Leads to High Fuel Production Rate, Large Light-to-Fuel Efficiency, and Excellent Durability for Photothermocatalytic CO_2 Reduction. *Adv. Energy Mater.* **2020**, *10*, 2002602. doi:10.1002/aenm.202002602.
147. Du Z, Pan F, Yang X, Fang L, Gang Y, Fang S, et al. Efficient photothermochemical dry reforming of methane over Ni

supported on ZrO_2 with CeO_2 incorporation. *Catal. Today* **2023**, *409*, 31–41. doi:10.1016/j.cattod.2022.05.014.

148. Haghshenas Y, Wong WP, Gunawan D, Khataee A, Keyikoğlu R, Razmjou A, et al. Predicting the rates of photocatalytic hydrogen evolution over cocatalyst-deposited TiO_2 using machine learning with active photon flux as a unifying feature. *EES Catal.* **2024**, *2*, 612–623. doi:10.1039/D3EY00246B.
149. Benavides-Hernández J, Dumeignil F. From Characterization to Discovery: Artificial Intelligence, Machine Learning and High-Throughput Experiments for Heterogeneous Catalyst Design. *ACS Catal.* **2024**, *14*, 11749–11779. doi:10.1021/acscatal.3c06293.